RSC Advances

PAPER

View Article Online
View Journal | View Issue

Cite this: *RSC Adv.*, 2025, **15**, 29753

Hybrid nucleobase–heterocycle–2-oxindole scaffolds as innovative cell cycle modulators with potential anticancer activity

Gehan Ahmed Abdel-Hafez,[a] Dagmara Kłopotowska,[b] Beata Filip-Psurska,[b] Ahmed S. Aboraia,[c] Joanna Wietrzyk,[b] Tarek Aboul-Fadl *[c] and Adel F. Youssef [c]

A series of hybrid molecules **6a–6d–13a–13d** combining pyrazolo[3,4-*d*]pyrimidine or aminopurine frameworks with an oxindole moiety were designed as multitarget anticancer agents. Several compounds, especially **8b** and **12a–12d**, showed potent antiproliferative effects against three human cancer cell lines: A498 (kidney carcinoma), HepG-2 (hepatocellular carcinoma), and MDA-MB-231 (breast adenocarcinoma). Compounds **6b**, **7b**, **8b**, and **12a–12c** exhibited remarkable CDK6 inhibition (pIC_{50} of up to 7.17), outperforming palbociclib, and VEGFR-2 inhibition comparable to sorafenib. These compounds also inhibited xanthine oxidase. Notably, **12a** and **12c** induced sub-G1 cell cycle arrest in HepG2 cells. Molecular modeling confirmed stable binding to CDK6 and VEGFR-2, while *in silico* ADMET profiling suggested favorable pharmacokinetics. These results support **8b** and **12a–12c** as strong leads for further multitarget cancer therapy development.

Received 12th July 2025
Accepted 6th August 2025

DOI: 10.1039/d5ra04997k

rsc.li/rsc-advances

Introduction

Cancer is a major global health and economic burden, causing nearly one in six deaths worldwide.[1,2] By 2050, more than 35 million new cases are projected due to population growth and aging.[3] Current treatment generally involves surgery, radiation, and chemotherapy, which face challenges like drug resistance and severe side effects. There is a pressing need for new anticancer agents with greater efficacy and lower toxicity. A deeper understanding of cell cycle control, particularly key checkpoints (late G1, G2/M, and metaphase-to-anaphase transition), offers a promising strategy for developing more effective cancer therapies.[4]

Cyclin-dependent kinases (CDKs) are serine/threonine protein kinases that regulate the cell cycle by forming heterodimeric complexes with cyclin subunits. Dysregulation of CDK or cyclin levels is frequently observed in cancers.[5,6] Among these, CDK4 and CDK6 are critical drivers of oncogenesis in specific tumors, making them promising targets for therapeutic development. Cyclin D-CDK4/6 complexes promote the transition from the G1 phase to the S phase by phosphorylating the retinoblastoma (RB) tumor suppressor protein, thereby facilitating cell cycle progression.[7–10] Inhibiting CDK4 and CDK6 is essential for targeting this critical cell cycle phase. Selective CDK4/6 inhibitors have shown effectiveness in treating various cancers, including melanoma, breast cancer, osteosarcoma, bladder cancer, lung cancer, and stomach cancer while minimizing toxicity in non-cancer cells. This therapeutic strategy holds promise for improving cancer treatment outcomes.[11–14] Various reported CDK4/6 inhibitors are based on various molecular scaffolds that enable specific binding to these kinases, thereby blocking their activity. Several "ciclib" scaffolds have been identified as core structural frameworks in the development of CDK4/6 inhibitors[15,16] are shown in Fig. 1. The pyrido[3,4-*d*]pyrimidin-4-one scaffold has been extensively explored for the development of experimental CDK4/6 inhibitors. Its core structure offers flexibility for optimizing its affinity towards CDK4/6, enabling the creation of selective inhibitors with varied pharmacokinetic properties. One of the first notable examples is palbociclib I,[17] which became the first FDA-approved CDK4/6 inhibitor. Dalpiciclib V is another potent and orally bioavailable CDK4/6 inhibitor, which differs from palbociclib by featuring a piperidine ring in place of the piperazine ring.

The pyrrolo[2,3-*d*] pyrimidine scaffold is represented by ribociclib II, the second FDA-approved oral CDK4/6 inhibitor. Birociclib VI is another selective CDK4/6 inhibitor containing this scaffold that has also gained FDA approval.[18,19]

The 6-(pyrimidin-4-yl)-1*H*-benzo[*d*]imidazole scaffold is exemplified by abemaciclib III, an oral CDK4/6 inhibitor, approved by the FDA. BPI-16350 VII is a highly potent CDK4/6 inhibitor with structural similarity to abemaciclib.[20] Finally, the tricyclic lactam scaffold underlies trilaciclib IV, the first

[a]*Medicinal Chemistry Department, Faculty of Pharmacy, Merit University, Sohag, Egypt*

[b]*Department of Experimental Oncology, Hirszfeld Institute of Immunology and Experimental Therapy, Polish Academy of Sciences, Wrocław, 53-114, Poland*

[c]*Medicinal Chemistry Department, Faculty of Pharmacy, Assiut University, Assiut, 71526, Egypt. E-mail: gehanahmed@aun.edu.eg; Fadl@aun.edu.eg*

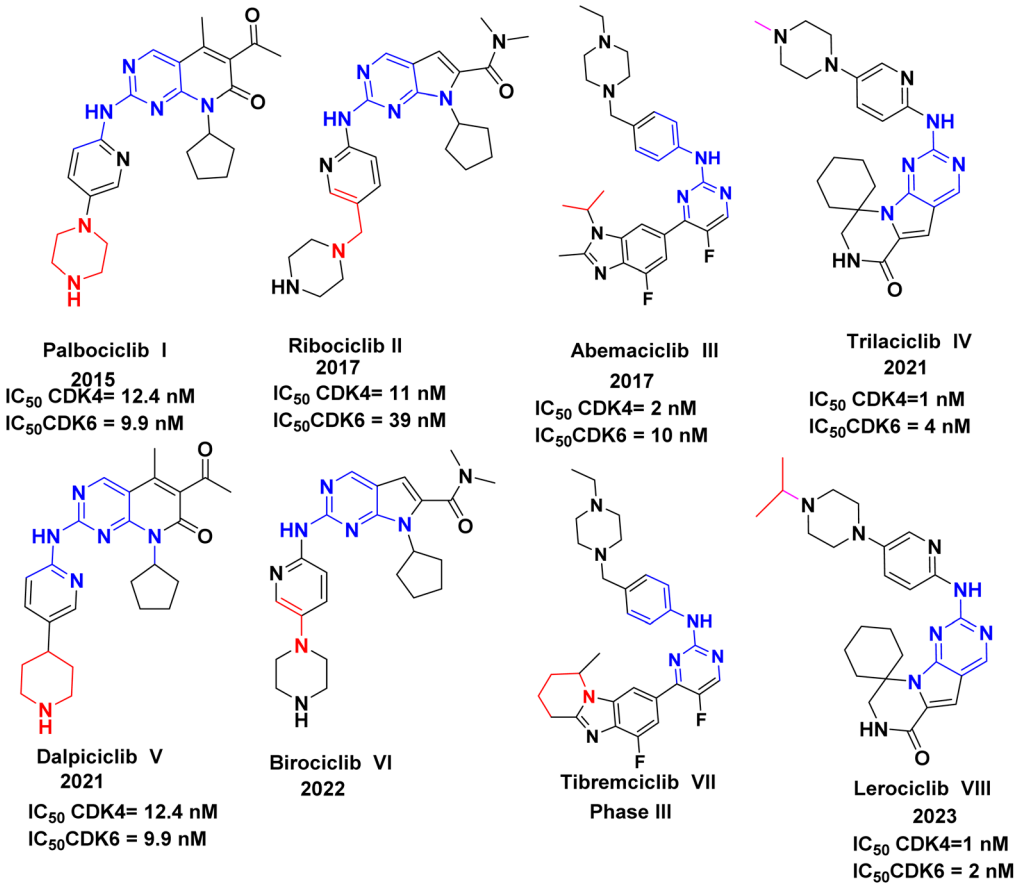

Fig. 1 Representative scaffolds of some reported CDK4/6 inhibitors.

FDA-approved CDK4/6 inhibitor for chemotherapy-induced myelosuppression. Lerociclib VIII, a structural analog of trilaciclib, is equally potent and selective for CDK4/6.

Vascular endothelial growth factor receptors (VEGFRs) are crucial receptor protein tyrosine kinases involved in tumor-induced angiogenesis, which are essential for tumor growth, progression, and metastasis.[21] Targeting the VEGFR-2 signaling pathway is a promising cancer therapy strategy, with FDA-approved VEGFR-2 inhibitors, like the "nibs" sorafenib, foretinib, regorafenib, and tivozanib.[22–24]

Xanthine oxidase (XO) overexpression is linked to cancer due to its role in generating reactive oxygen species (ROS) and activating carcinogens. XO oxidizes hypoxanthine to xanthine and uric acid, producing ROS that promote tumor progression, inflammation, angiogenesis, and cell migration. XO inhibitors can suppress proinflammatory and proapoptotic proteins, potentially aiding cancer treatment. Elevated uric acid levels correlate with poorer survival rates in cancer patients, highlighting XO as a diagnostic and prognostic marker. Although XO inhibitors reduce oxidative stress and inflammation, their impact on cancer progression and metastasis remains largely unexplored.[25,26]

Current studies focus on developing next-generation inhibitors targeting CDK4/6, VEGFR-2, and XO. These targets are critical in cancer progression, with CDK4/6 regulating the cell cycle, VEGFR-2 facilitating angiogenesis, and XO generating ROS.[27] By targeting all three, it may be possible to enhance anticancer efficacy by inhibiting cell proliferation and tumor blood supply. Specific chemical scaffolds, such as oxindoles, purines, pyrimidines, and pyrazolopyrimidines, are explored for their biological activities. Oxindoles exhibit anticancer properties by inhibiting key enzymes, with C3-substituted derivatives enhancing interactions for novel drug design. FDA-approved oxindole-based drugs, like sunitinib and nintedanib, treat renal cell carcinoma and adenocarcinoma, while indirubin shows CDK inhibition, and toceranib is used in veterinary oncology. Other oxindole inhibitors are orantinib and target receptor tyrosine kinases.[28,29] Additionally, thiazolidinone and thiazolylidene derivatives, featuring an –N=C–S– moiety, display diverse biological activities, with ponesimod gaining FDA approval for multiple sclerosis.[30,31] Purines and pyrimidines, which are fundamental to DNA and RNA, are crucial in drug discovery. Purine derivatives serve as anticancer antimetabolites, while pyrimidines exhibit diverse biological activities. Targeting nucleotide synthesis with analogs enhances chemotherapy.[32] Pyrazolopyrimidines serve as bioisosteres of adenine, mimic ATP interactions, and function as CDK inhibitors. Allopurinol, a pyrazolopyrimidine, inhibits xanthine oxidase and exhibits cytotoxic effects. Its structural versatility and tautomeric forms enhance its therapeutic potential.[33,34] In this

framework, structure-based drug design (SBDD) and molecular docking were performed to evaluate the binding affinities of the designed compounds within the active site of CDK6, a key enzyme in cancer progression. Their affinities were compared with palbociclib to validate the design strategy.

Design rational

A novel series of compounds incorporating pyrazolo[3,4-*d*] pyrimidine and aminopurine scaffolds, fused with an oxindole ring, was strategically designed to inhibit CDK6, VEGFR-2, and xanthine oxidase, which are critical enzymes involved in cancer progression. The structural design of these compounds focuses on enhancing both potency and multi-targeted therapeutic effectiveness and is summarized as follows (Fig. 2).

(1) Scaffold modification

The pyrido[3,4-*d*] pyrimidine scaffold of palbociclib was replaced with pyrazolo[3,4-*d*] pyrimidine and aminopurine, combined with an oxindole ring. This adjustment enables noncovalent bonding with Val101 and Asp163 in the CDK6 active site.

(2) Oxindole substitutions

Variably substituted oxindole rings incorporating electron-donating (EDGs) and electron-withdrawing groups (EWGs) were designed to evaluate the effects of electronic modifications on biological activity.

(3) Thiosemicarbazide addition

A thiosemicarbazide motif was attached at the oxindole's C-3 position to boost the potency of the target compounds.

(4) Thiosemicarbazone cyclization

Cyclized forms, such as 2-hydrazinylidine thiazolidin-4-one and 2-hydrazinylidine-2,3-dihydrothiazole, were introduced at oxindole's C-3 position to enhance binding affinity and potency *via* alternative interactions.

These design elements maximize structural diversity and binding efficiency, paving the way for novel multi-targeted cancer therapies.

Results and discussion

Computational studies

Molecular docking of the design compounds onto the CDK4/6 inhibitor. In our study, we focused on developing new compounds that target the ATP binding site of the CDK6 enzyme. Our approach was inspired by the structural analysis of palbociclib, a known CDK6 inhibitor, which was studied in complex with the enzyme (PDB ID: 5L2I).[35] Fig. 3 shows how palbociclib binds to the ATP active site, serving as a foundation for designing improved CDK6 inhibitors.

Docking studies for the newly designed compounds **6a–6d**–**13a–13d** were conducted using MOE 2020.01 software, utilizing the three-dimensional structure of the CDK6 enzyme in complex with palbociclib, obtained from the Protein Data Bank (PDB).

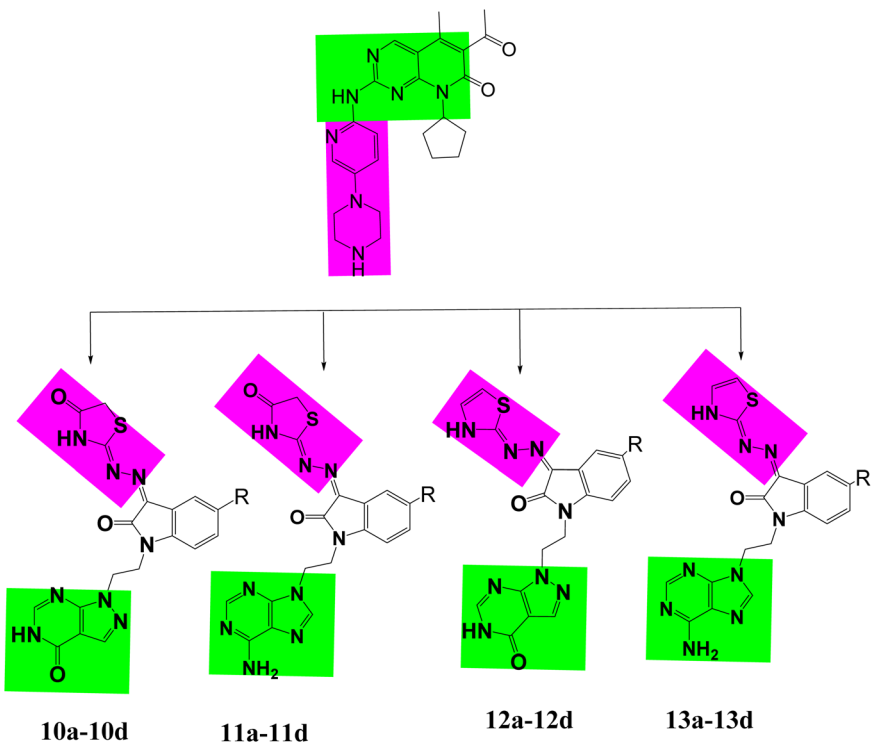

Fig. 2 Feature similarities of the palbociclib ligand and the newly designed compounds **10a–d**–**13a–d** as potent CDK4/6 inhibitors.

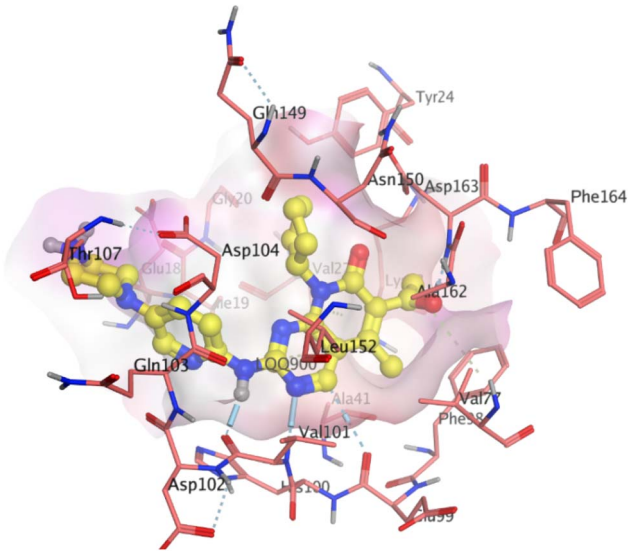

Fig. 3 Schematic of the binding regions within the ATP active site of CDK6 in complex with palbociclib. The key interaction regions are (1) hinge (adenine) region—Val101, Leu152, Glu99, and Phe98 residues; (2) ribose pocket—Asp163 and Lys43 residues; (3) hydrophobic region—Phe98 and Leu152 residues; (4) solvent region—Asp163 and Lys43 residues; and (5) phosphate pocket—Lys43, Asp145, and Glu61 residues.

To ensure the accuracy of the docking protocol, palbociclib was redocked into the CDK6 active site, yielding a root-mean-square deviation (RMSD) of 1.03 Å and a binding score of -8.23 kcal mol^{-1}. The docking procedure successfully reproduced all key interactions observed in the co-crystallized structure, confirming the reliability of the methodology. This validated approach was then employed to investigate the binding interactions of the newly designed compounds, allowing for a comparative analysis of palbociclib within the active site. The co-crystal structure of CDK6 with palbociclib revealed strong interactions within the ATP binding site, contributing to the compound's stability and selectivity. Palbociclib is anchored by three key hydrogen bonds: two with Val101 in the hinge region and one with Asp163 in the DFG (Asp–Phe–Gly) motif. Additionally, it establishes a favorable electrostatic interaction with a solvent-exposed ridge formed by Asp104 and Thr107. Further stabilization is provided by multiple polar interactions between the ribose and phosphate groups and residues Val27 and Ala162. A defining feature of palbociclib is its high specificity for CDK4/6, with minimal activity against other CDKs or non-CDKs. This selectivity is largely attributed to interactions with CDK4/6-specific residues, particularly His100 and Thr107 near the hinge region. Notably, His100 is exclusive to CDK4 and CDK6, further reinforcing its specificity. Additionally, kinase selectivity may be influenced by palbociclib's lipophilicity, as its cLog *P* value facilitates deeper accommodation within the ATP-binding cleft (Fig. S1, SI).

The designed compounds **6a–6d–13a–13d** exhibited a common binding pattern, forming halogen bonds (XB) and/or hydrogen bonds (HB) with Val101, along with hydrogen bonding interactions with Asp163 residues in the hinge (adenine) region, which are critical for CDK6 inhibition. Additionally, these compounds engage in hydrophobic interactions with key gatekeeper residues, including Phe98, Val27, and Ile19. Beyond these core interactions, the new compounds also formed additional contacts with amino acids, such as Asp104, Asn150, Gln149, Gly20, Gly165, Leu96, Leu152, Leu166, Lys43, Lys147, Phe164, and Val77. These extended interactions, facilitated by the molecular design, contributed to the overall stability of the ligand–protein complex. Several compounds, specifically **8b**, **9b**, **10a–10c**, **11b**, **12a–12d** and **13c–13d**, demonstrated binding scores ranging from ΔG -8.29 to -9.00 kcal mol^{-1}, surpassing the binding score of palbociclib (-8.23 kcal mol^{-1}). In contrast, compounds **6a–6d** and **7a-7d** exhibited lower binding scores, ranging from -6.95 to -7.45 kcal mol^{-1}. However, these compounds still showed an affinity for the ATP binding site of CDK6 by interacting with Val101 and Asp163 and penetrating the ribose pocket through interactions with Leu152, Leu166, and Phe164, as exemplified by compounds **6b** and **7b** (Fig. 4). These findings support the synthesis of docked compounds and encourage further evaluation of their potential as CDK6 inhibitors.

Thiosemicarbazone groups **8a–8d** and **9a–9d** showed slightly better binding energy, ranging from -7.71 to -8.35 kcal mol^{-1},

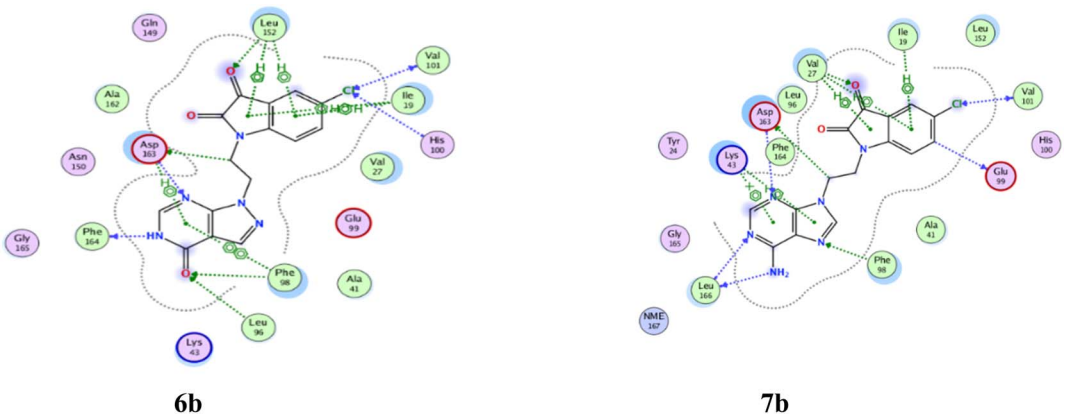

Fig. 4 2D interaction of the designed compounds **6b** and **7b**.

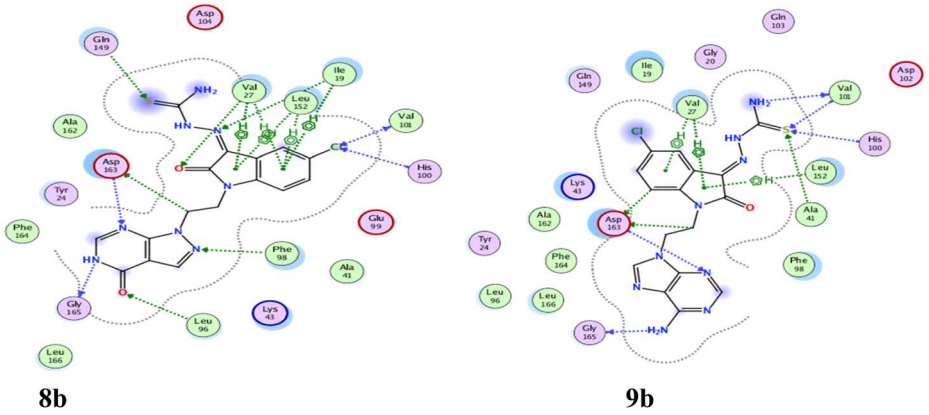

Fig. 5 2D interaction of the designed compounds **8b** and **9b**.

due to their interaction with essential amino acids Val101 and His100, which matched the binding interaction with palbociclib. Additionally, they bind to extra amino acids, including Leu96, Gln149, Leu152, and Gly165, as depicted in Fig. 5. The higher ΔG of **8b** was attributed to the strong electrostatic Cl···O attraction ($d = 3.14$ Å) contributed to CDK6 inhibition activity.

The thiazolidinone moiety of compounds **10a–10d** and **11a–11d** binds to the crucial amino acids Val101 and Glu99, plus the added interactions with Asn150, Asp 104, Leu96, Leu152, Gly20, Gly 165, and Tyr24. These compounds exhibit a higher binding energy than palbociclib. The sulphur atom within the thiazolylidene moiety in **12a–12d** and **13a–13d** binds in hydrogen bonding with the solvent region of the CDK6 enzyme's active site, particularly with Asp104. Meanwhile, the thiazolylidene moiety is positioned toward the ribose pocket, facilitating hydrophobic interactions with Gly20. These compounds not only bind to crucial amino acids but also interact with additional residues, like Leu96, Leu166, Phe164, Val77, Gln149, and Gly165. They exhibit the highest binding scores of ΔGs of **12a–12d** and **13a–13d** among the compounds studied, as shown in Fig. 6.

The 5-chloro-substituent plays a significant role in binding to the CDK6 enzyme's active site. Among the designed compounds, variations at the 5-position include H, Cl, OCH_3, and F. Notably, compounds featuring 5-chloro substituents exhibit the most favorable binding interactions with the CDK6 enzyme's active site, particularly through interactions with essential residues Val101 and His100. Representative examples of compounds **6b**, **6c** and **6d** contain similar structural substituents but differ solely in the 5-position, Fig. S2, SI.

To assess the selectivity of the newly designed compounds for CDK6 over CDK2, docking studies were conducted using the CDK2-sunitinib complex (PDB ID: 3TI1). The results showed that the tested compounds exhibited different binding modes compared to sunitinib, which interacts with CDK2 through hydrogen bonding with Glu81 and Leu83 in the ATP-binding site, along with hydrophobic interactions involving Phe80, Ile10, and Asp86.

The tested compounds displayed interaction energies ranging from $\Delta G = -7.07$ to -8.23 kcal mol^{-1}, while the lead compounds had a slightly stronger interaction energy of $\Delta G = -8.65$ kcal mol^{-1}. Notably, compounds **8b**, **12a–12c**, and **13b**

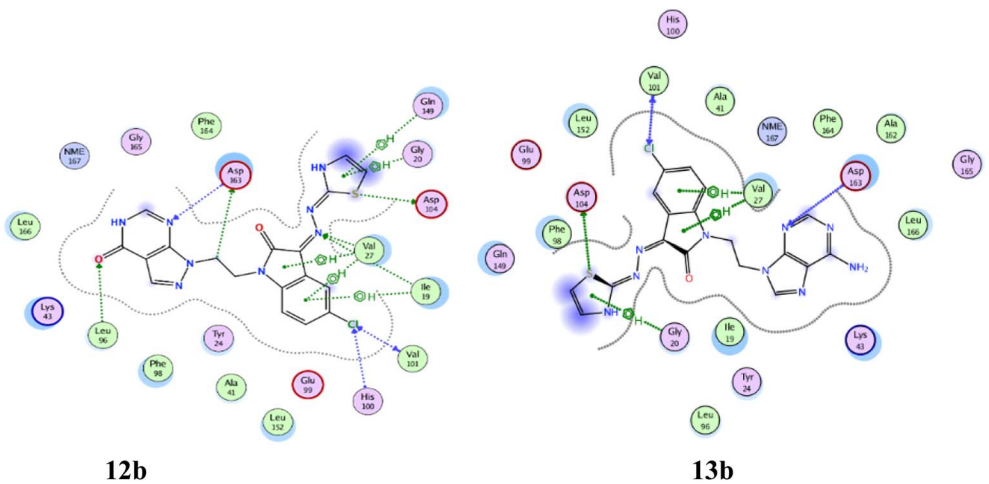

Fig. 6 2D interaction of the designed compounds **12b** and **13b**.

Table 1 Binding energy score of the docked most active cytotoxic compounds on VEGFR-2

Compound	Binding score ΔG (kcal mol^{-1})	Amino acids involved in interaction
Sorafenib	−10.16	Asp1046, Glu885, Cys919, Phe1047, Leu840 and Leu1035
6b	−7.68	Asp1046, Glu885, Leu889, Cys1045 and Phe1047
7b	−7.33	Glu885, Cys1024, Leu889, Ile888, and His1026
8b	−9.13	Asp1046, Glu885, Cys919, Cys1045, Leu840 and Lys868
12a	−8.99	Asp1046, Glu885, Cys1045, Leu889, Ile888, Cys1024 and Arg1027
12b	−8.84	Asp1046, Glu885, Cys1045, Leu889 and Ile888
12c	−8.13	Asp1046, Glu885, Ile888, Cys1024, Ile1025 and Arg1027
13b	−7.89	Asp1046, Leu889, Ile888, Glu815, His816 and Lys868

failed to establish crucial hydrogen bonds with Leu83 and lacked hydrophobic interactions with Phe80. Similarly, compounds **6b** and **7b** did not form key hydrogen bonds with Leu83 or interact hydrophobically with Phe80. These findings suggest that the designed compounds exhibit distinct binding preferences, reinforcing their selectivity for CDK6 over CDK2 (Fig. S3, SI).

Docking studies of the VEGFR-2 inhibitor. Docking studies were conducted on the most active compounds **6b**, **7b**, **8b**, **12a–d**, and **13b** using the VEGFR-2 co-crystal structure with sorafenib (PDB ID: 3WZE)[36–39] and MOE 2020.01 software. The docking protocol was validated by redocking sorafenib into the VEGFR-2 active site, which yielded an RMSD of 1.02 Å and a binding score of −10.16 kcal mol^{-1}, successfully reproducing key interactions with critical binding site residues (Table 1). Sorafenib interacts with VEGFR-2 through five hydrogen bonds: two with Cys919, two with Glu885, and one with Asp1046. Its *N*-methyl picolinamide group fits into a pocket formed by Cys919, Phe918, Leu1035, Lys920, Glu917, Val848, and Leu889, while the terminal 3-trifluoromethyl-4-chlorophenyl group occupies a hydrophobic channel involving residues such as Phe1047, Cys1045, and Ile1044. The urea spacer plays a key role in binding, enhancing sorafenib's affinity for VEGFR-2 (Fig. 7). These findings highlight the potential of modifying linker structures to develop more potent VEGFR-2 inhibitors.

Compound **8b** exhibited a binding mode closely resembling that of sorafenib, with a binding score of −9.00 kcal mol^{-1} and the formation of five hydrogen bonds. The pyrazolopyrimidine ring forms one hydrogen bond with Cys919, while the hydrazino groups establish three hydrogen bonds with Asp1046, Cys1045, and Glu885. Additionally, the sulfur atom of the thiosemicarbazide moiety forms a hydrogen bond with Lys868. The 1-ethyl pyrazolo pyrimidine scaffold fits into a pocket formed by Leu1035, Lys920, Cys919, Phe918, Glu917, Ala866, and Val848, while the terminal thiosemicarbazone tail occupies a hydrophobic channel created by Phe1046, Ile1044, Val916, Val914, and Leu889 (Fig. S4, SI). These key interactions likely contributed to the strong anticancer activity of compound **8b**.

The predicted binding mode of compound **12a** closely resembles that of sorafenib and **8b**, with a binding score of −8.95 kcal mol^{-1} and four hydrogen bonds. The pyrazolopyrimidine ring forms hydrogen bonds with Cys1024 and Ile888, while the ethylene linker interacts with Asp1046. Additionally, the NH group of the thiazolylidene forms a hydrogen bond with Glu885, and the sulfur atom establishes another with Cys1045. The 1-ethyl pyrazolopyrimidine and oxindole scaffolds fit within a hydrophobic pocket composed of Arg1027, Ile1025, Leu1019, Ile892, Leu889, and Glu815, while the terminal thiazolylidene tail is accommodated in a hydrophobic channel formed by His1026, Val916, Val899, Val898, and Lys898 (Fig. S5, SI).

Compound **12b** displayed a binding score of −8.84 kcal-mol^{-1} and formed three hydrogen bonds. The ethylene linker interacts with Asp1046, while the NH group and sulfur atom of the thiazolylidene form hydrogen bonds with Glu885 and Cys1045, respectively. Its 1-ethyl pyrazolopyrimidine and oxindole scaffold occupy a hydrophobic pocket consisting of

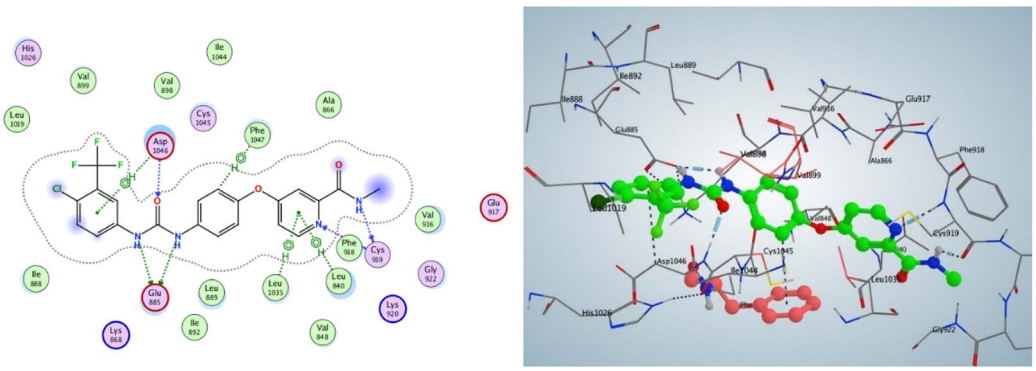

Fig. 7 2D and 3D interactions of co-crystallized sorafenib shown in green and red, adopting the Phe1047 "DFG-out" conformation.

Arg1027, Cys1024, Ile1025, Leu1019, Ile892, Leu889, Lys868, and Glu815. Terminal thiazolylidene tail is positioned within a hydrophobic channel formed by Ile1044, His1026, Val916, Val899, and Val898 (Fig. S6, SI).

These docking results suggest that the linkers used in these compounds align with the urea linker in sorafenib, serving a similar function and enhancing affinity for the VEGFR-2 enzyme. The formation of hydrogen bonds with Cys919, Asp1046, and Glu889, along with key hydrophobic interactions, likely contributes to the strong binding of the heterocyclic pyrazolopyrimidine scaffold to VEGFR-2.

Molecular dynamics simulation

Compound **12b** exhibited good stability within the CDK6 active site, maintaining an average RMSD of 2.5489 Å, which is comparable to palbociclib (2.4922 Å) (Fig. S7, SI). The interaction energies further supported this stability, with total electrostatic and van der Waals energies of −40.17 kcal mol^{-1} for **12b** and −36.94 kcal mol^{-1} for palbociclib. Both compounds formed hydrogen bonds with key residues, contributing to their stable binding (Fig. S8 and S9, SI). MM-PBSA calculations revealed that **12b** had a slightly better binding free energy (−9.3551 kcal mol^{-1}) than palbociclib (−9.0804 kcal mol^{-1}), aligning with its *in vitro* inhibitory activity (IC_{50} = 0.123 μM). Protein stability assessments showed similar RMSD values (**12b**: 2.2934 Å, palbociclib: 2.2148 Å) (Fig. S10) and RMSF values (**12b**, 1.5675 Å; palbociclib, 1.6492 Å) profiles (Fig. S11), indicating the structural stability of the protein. Additional parameters, including the radius of gyration (**12b**: 19.42 Å, palbociclib: 19.47 Å) (Fig. S12 and S13) and solvent-accessible surface area (SASA ∼ 14 360 $Å^2$) (Fig. S14), further confirmed the compactness and stability of the CDK6 complexes.

Overall, the 50 ns molecular dynamics simulation demonstrated that compound **12b** exhibits strong stability and binding affinity, highlighting its potential as a potent CDK6 inhibitor (Fig. 8 and 9).

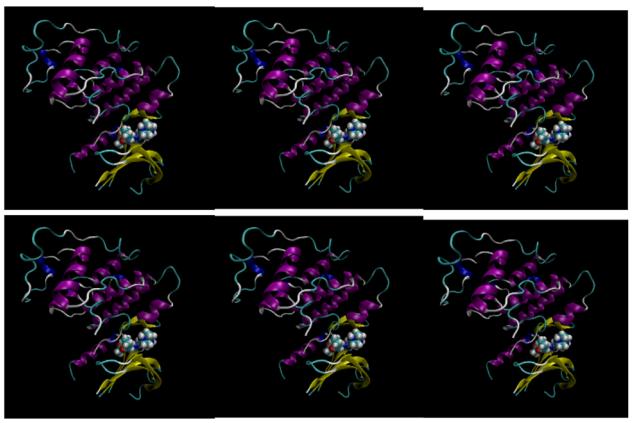

Fig. 8 Snapshots of palbociclib inside the active site of CDK6 over 50 ns long MDS (5, 10, 20, 30, 40 and 50 ns).

Chemistry

Target molecules **6a–d–13a–d** were synthesized as outlined in Scheme 1, and their structures were confirmed through spectral analyses (Fig. S15–S30).

It has been reported that the reaction of isatin with thiosemicarbazide is stereoselective, producing only the *Z*-diastereomer. The chemical shifts of the synthesized compounds **8a–8d–9a–9d** are comparable with the reported ^{1}H NMR of *Z*-thiosemicarbazone[40,41] (Fig. S31–S46). These compounds exhibit highly deshielded hydrazine protons resonated at a far downfield shift around δ 12.22–12.09 ppm stemming from the strong intramolecular hydrogen bond formed with the lactam oxygen atom of oxindole (N···H···O d = 2.09 Å, and Φ = 130°) to stabilize the *Z* configuration,[42] as depicted in Fig. 10.

The cyclization of the $SCNH_2$ moiety was performed using ethyl bromoacetate and a catalytic amount of anhydrous sodium acetate, yielding oxindole-allopurinol-2-hydrazonothiazolidin-4-one **10a–10d**. Alternatively, cyclization

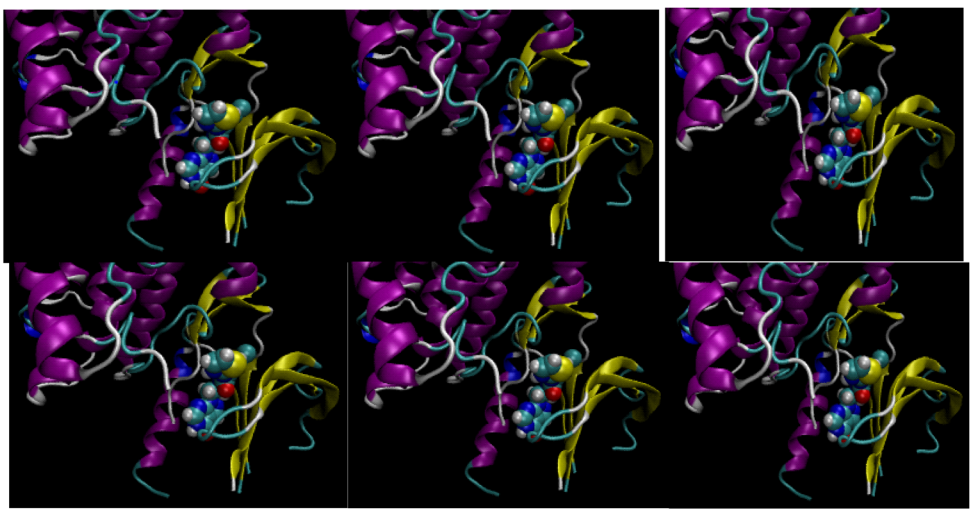

Fig. 9 Snapshots of compound **12b** inside the active site of CDK6 over 50 ns long MDS (5, 10, 20, 30, 40 and 50 ns).

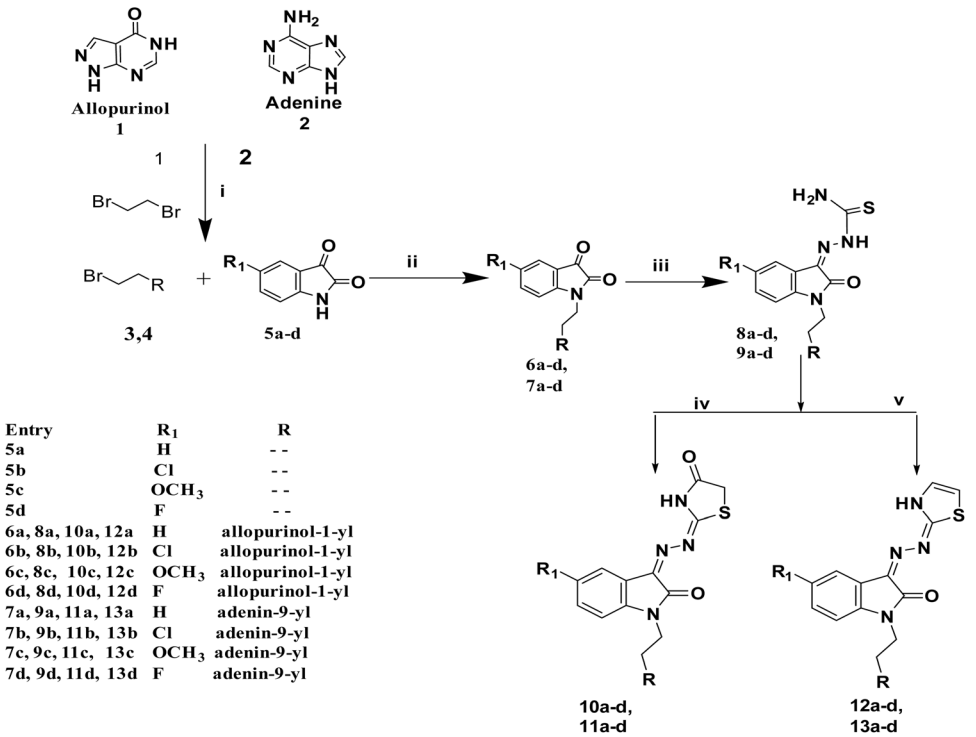

Entry	R_1	R
5a	H	- -
5b	Cl	- -
5c	OCH_3	- -
5d	F	- -
6a, 8a, 10a, 12a	H	allopurinol-1-yl
6b, 8b, 10b, 12b	Cl	allopurinol-1-yl
6c, 8c, 10c, 12c	OCH_3	allopurinol-1-yl
6d, 8d, 10d, 12d	F	allopurinol-1-yl
7a, 9a, 11a, 13a	H	adenin-9-yl
7b, 9b, 11b, 13b	Cl	adenin-9-yl
7c, 9c, 11c, 13c	OCH_3	adenin-9-yl
7d, 9d, 11d, 13d	F	adenin-9-yl

Scheme 1 Synthesis of the target compounds **6a–d–13a–d**. (i) K_2CO_3, 1,2-dibromoethane, DMF, r.t., 24 h; (ii) K_2CO_3, DMF, 60 °C, 6–8 h; (iii) thiosemicarbazide, EtOH, reflux, 2–4 h; (iv) ethyl bromoacetate or monochloroacetic acid, sod. acetate, EtOH, reflux, 24 h; and (v) chloroacetone, sod. acetate, EtOH, reflux, 24 h.

in the presence of monochloroacetic acid resulted in oxindole-adenine-2-hydrazonothiazolidin-4-one **11a-11d**.

Further modification of the $SCNH_2$ cyclization polarity was achieved using chloroacetone, leading to the formation of oxindole-allopurinol/adenine thiazol-2(3*H*)-ylidenes **12a–12d** and **13a–13d**. The structures and purity of the synthesized compounds were confirmed through spectral and elemental analyses (Fig. S47–S77).

As expected, the restricted rotation of the thiazolylidene ring and the imine group in **12a–12d** and **13a–13d** revealed *E* and *Z* diasteroisomers. The proton peaks of the *E*-diastereomer are significantly downfield shifted relative to those of the *Z*-diastereomer. For example, in the ^{1}H-NMR spectrum of compound **13a** *E*/*Z*%, 38 : 62, the formation of the thiazolyidene ring is confirmed by the presence of two characteristic singlet peaks for **SCH$_{(E)}$** and **SCH$_{(Z)}$** at 6.51 and 6.36 ppm, respectively. Additionally, two characteristic doublet peaks were assigned to **NCH$_{(E)}$** and **NCH$_{(Z)}$** at 7.15 and 6.89 ppm, respectively. The chemical shift of the indole proton at C4H is particularly useful for differentiating between *E*- and *Z*-diastereomers. The C4H proton of the *E*-diastereomer resonates more downfield, appearing as a doublet around δ 8.26 ppm, while the C4H proton of the *Z*-diastereomer resonates relatively upfield, appearing as a doublet around δ 7.48 ppm. The same pattern was observed in ^{13}C-NMR spectra, **NCH$_{(E)}$** and **NCH$_{(Z)}$**, around δ 122.8 and 121.8 ppm, respectively, and was observed in **C4$_{(E)}$** and **C4$_{(Z)}$** around δ 130.0 and 129.5 ppm, respectively. The differentiation of *E*- and *Z*-diastereomers can be effectively achieved using 2D-NMR techniques. The ^{1}H–^{1}H NOESY experiment confirmed the presence of both diastereomers (*E*/*Z*) in isatin-thiazol-2(3*H*)ylidene, enabling the assignment of *E* and *Z* protons. As a representative example, compound **10b** exhibited no NOE cross-peak between the NH and C4–H protons, indicating that these groups are spatially separated and oriented differently. Additionally, the presence of cross-peaks between the C7–H and N1–CH_2 protons of oxindole further supports the *Z*-configuration of compound **10b**, which can be extrapolated to other derivatives, as illustrated in Fig. 11.

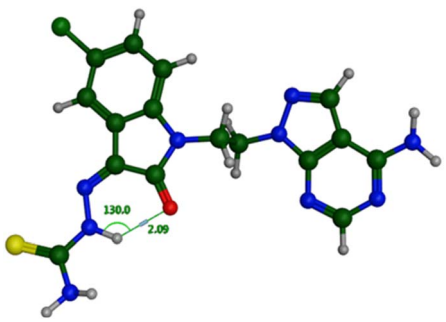

Fig. 10 Representative example for the *Z* configuration of **9b**.

The purity of the synthesized compounds was confirmed by elemental analysis, with deviations within acceptable limits (±0.4%). Furthermore, HPLC chromatograms of representative compounds **6b**, **8b**, **12a**, **12b**, and **12c**, using allopurinol as an internal standard, indicated high chemical purity, with all

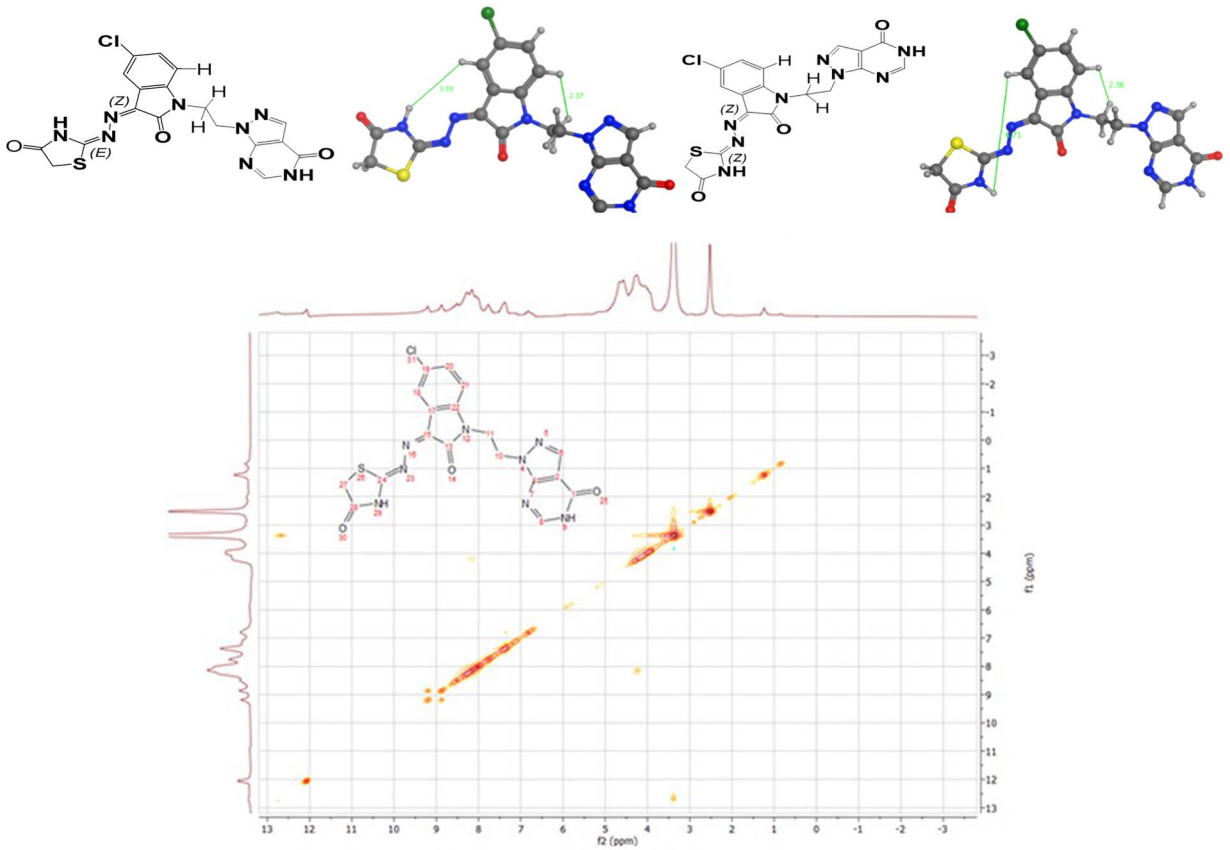

Fig. 11 $^{1}H-^{1}H$-NOESY spectrum of compound **10b**.

tested leads showing purity ≥95% and several exceeding 97% at their respective retention times. These findings confirm the successful synthesis and isolation of highly pure compounds suitable for subsequent biological studies and formulation efforts. Detailed chromatographic data are provided in the SI (Fig. S78–S82).

Biological evaluation

Antiproliferative activity assay

The antiproliferative activities of allopurinol-isatin and adenine-isatin derivatives **6a–6d** and **7a–7d**, along with thiosemicarbazone derivatives **8a–8d** and **9a–9d**, and cyclized products 2-hydrazinylidine thiazolidin-4-one **10a–10d** and **11a–11d**, as well as 2-hydrazinylidine-2,3-dihydrothiazole **12a–12d** and **13a–13d**, were evaluated against three cancer cell lines: A498 (kidney carcinoma), HepG-2 (hepatocellular carcinoma), and MDA-MB-231 (breast adenocarcinoma). Additionally, their effects on the normal murine embryonic fibroblast cell line BALB/3T3 (clone A31) were assessed using the sulforhodamine B (SRB) assay to determine antiproliferative activity compared to the reference drug sorafenib. The results shown in Tables 2, S1 and Fig. S83 clearly reveal that most of the synthesized compounds have pIC_{50} in the range of 4.03–5.82, matching or higher than the reference sorafenib. Of these active compounds, 30 structures carry the allopurinol feature and nine carry the adenine. Among series **6a–6d** and **7a–7d**, the most active ligands are those with a higher lipophilic nature, carrying 5-chloroindoline-2-one fragment **6b** (clog $P = 0.77$) and **7b** (clog $P = 1.54$). The allopurinol compound **6b** R_1 = Cl showed the most distinct effect against the three cancer cell lines pIC_{50} (4.79, 4.82, and 4.88), and in the adenine, series **7b** showed antiproliferative effects against HepG2 and MDA-MB-231 pIC_{50} (5.22 and 4.71, respectively). Both most probably privileged the contribution of halogen bond formation that improved the binding affinity of ligands to the residues in the active site compared to **6d** pIC_{50} (4.21, 4.32, and 4.41) and **7d** with promising activity against the three cancer cell lines pIC_{50} (3.78, 4.76, and 4.08).

However, the other substituents H and OMe in **6a**, **6c**, **7a** and **7c** displayed relatively lower potency against the three cell lines.

The attachment of the thiosemicarbazide fragment to the ligands **6a–6d** and **7a–7d** demoted the scope and potency of the produced thiosemicarbazones against the three cancer cell lines. Nonetheless, the thiosemicarbazones **8b**, **8d**, and **9c** showed *potent antiproliferative activity* pIC_{50} (4.53–4.88) against the A-498 and HepG2 cell lines. Further modifications of **8a–8d** and **9a–9d** were conducted *via* two cyclization reactions of the $SCNH_2$ moiety. The first cyclized moiety was 2-hydrazinylidenethiazolidin-4-ones **10a–10d** and **11a–11d**. Incorporation of the lactam scaffold resulted in a reduction of one hydrogen bond donor (HBD) and an increase of two

Table 2 Antiproliferative activity of the synthesized compounds against A-498, HepG2, and MDA-MB-231 tumor cell lines using SRB assay with sorafenib as a positive control

		pIC_{50}[b]				pIC_{50}[b]		
Entry	R_1	A-498	HepG2	MDA-MB-231	Entry	A-498	HepG2	MDA-MB-231
6a	H	4.23	3.82	4.04	**7a**	n.a.[a]	n.a.	3.68
6b	Cl	4.79	4.82	4.88	**7b**	4.28	5.22	4.71
6c	OCH_3	4.52	4.03	4.32	**7c**	3.74	4.11	3.87
6d	F	4.41	4.21	4.32	**7d**	3.78	4.76	4.08
8a	H	n.a.	n.a.	n.a.	**9a**	n.a.	n.a.	n.a.
8b	Cl	4.85	4.88	4.27	**9b**	n.a.	n.a.	n.a.
8c	OCH_3	n.a.	n.a.	n.a.	**9c**	n.a.	4.53	4.14
8d	F	3.98	4.60	n.a.	**9d**	n.a.	4.25	n.a.
10a	H	n.a.	n.a.	n.a.	**11a**	n.a.	n.a.	n.a.
10b	Cl	4.03	5.27	4.29	**11b**	n.a.	n.a.	n.a.
10c	OCH_3	n.a.	n.a.	n.a.	**11c**	n.a.	n.a.	n.a.
10d	F	n.a.	n.a.	n.a.	**11d**	3.72	n.a.	3.72
12a	H	5.12	5.82	5.35	**13a**	3.72	n.a.	n.a.
12b	Cl	5.29	5.76	5.41	**13b**	n.a.	n.a.	n.a.
12c	OCH_3	4.26	5.25	4.81	**13c**	3.98	3.84	3.75
12d	F	4.51	5.21	4.93	**13d**	3.85	3.72	n.a.
Sorafenib		4.20	4.35	4.09				

[a] n.a. – not active. [b] $pIC_{50} = -\log IC_{50}$ (molar concentration).

hydrogen bond acceptors (HBAs) per molecule relative to precursors **8a–8d** and **9a–9d**. The conversion of the $-SCNH_2$ functionality into a lactam framework led to a restricted antiproliferative profile and diminished cytotoxic potency when compared with the corresponding thiosemicarbazone analogues. An exception was **10b**, which displayed high potency ($pIC_{50} = 5.27$) against the HepG-2 cell line, and moderate potency against A-498 and MDA-MB-231 ($pIC_{50} = 4.03$ and 4.29, respectively). The other compounds in this series exhibited lower activity. This observed inconsistency is most probably attributed to the spatial orientation of the majority of the 2-iminothiazolidin-4-one moiety within the active site of the targeted cell lines, which favors the two effectors, allopurinol and 5-chloroxindole nuclei. To improve the activities of **10a–10d** and **11a–11d**, we intended to attenuate the polarity and to avoid the HBA motif provided by the O in the lactam fragment. This goal was fulfilled by the cyclization of the terminal $SCNH_2$ fragment following the procedure outlined in Scheme 1 to yield a series of allopurinol/adenine-oxindole 2-hydrazinylideno thiazole **12a–12d** and **13a–13d**. Fortunately, the antiproliferative potency and scope of action of the allopurinol series shown by **12a–12d** have surpassed the pIC_{50} of the reference drug sorafenib. The activities of **12a** and **12b** against A-498 are 2-fold, against HepG2 are 8-fold, and against MDA-MB-231 are 5-fold those of sorafenib, which exhibits low cytotoxicity towards BALB/3T3 cells, indicating safety for normal cells. The activities of **12c** and **12d** against A-498 are 8-fold, against HepG2 are 30-fold, and against MDA-MB-231 are 20-fold those of sorafenib. However, adenine series **13a–13d** showed marginal activity against any one of the cell lines. The observed strong anticancer activity of compounds **12a–12d** can be attributed to the robust interactions of the motifs attached to the terminals of the dimethylene linker, namely the pyrazolo pyrimidinone, on one hand, and the fragments attached to the oxindole nucleus, on the other hand, showing multiple binding forces in the active site of the CDK6 enzyme. This interaction is further supported by their high binding scores, confirming their strong affinity for the target.

The selectivity indices (SI) were calculated for the most active compounds using the ratio SI = (IC_{50} μM against normal cell line BALB/3T3)/(IC_{50} μM against respective cancerous cell line) to evaluate the toxicity of tested compounds against normal cells and to predict their therapeutic potential. A favorable SI > 1.0 indicates a drug with efficacy against tumor cells greater than the toxicity against normal cells. The most active compounds **6b**, **7b**, **8b** and **12a–12d** displayed an SI median of 2.8 against A498; against HepG2, **6a**, **7b**, and **8b** showed an SI median of 2.03; and against MDA-MB-231 compounds, **6b**, **7b** and **12b** showed an SI median of 2.49 (Table 3). The most active compounds with $pIC_{50} \geq 4.5$ showed SI values higher than the reference, which entitled them to further development as therapeutic candidates, especially for targeting the HepG2 cell line.

Table 3 SI of the most active compounds **6b**, **7b**, **8b**, **12a–d** and sorafenib

Entry	Selectivity index (SI)		
Cell lines	A498	HepG2	MDA-MB-231
6b	2.03	2.15	2.49
7b	1.37	11.89	3.64
8b	2.45	2.60	0.63
12a	0.59	2.95	1.00
12b	0.79	2.80	1.25
12c	0.29	9.92	0.99
12d	0.35	1.78	0.91
Sorafenib	0.014	0.02	0.011

Table 4 Cell cycle analysis results presented as the means of cell percentage [%] ± SD

	Cell percentage [%] ± SD			
Entry	SubG1	G0/G1	S	G2/M
Ctrl	7.12 ± 0.569	45.40 ± 3.051	24.54 ± 2.475	20.98 ± 0.614
6b, 1 μg mL^{-1}	3.48 ± 1.178	50.37 ± 4.619	27.15 ± 3.651	17.67 ± 1.285
7b, 10 μg mL^{-1}	6.15 ± 2.739	44.36 ± 4.193	36.66 ± 4.326	13.32 ± 2.763
12a, 1 μg mL^{-1}	31.28 ± 10.88	35.43 ± 5.182	24.34 ± 8.875	6.64 ± 2.959
12c, 1 μg mL^{-1}	21.16 ± 6.283	38.41 ± 4.391	29.22 ± 4.063	10.59 ± 1.830

Cell cycle analysis

Cell cycle distribution for compounds **6b**, **7b**, **12a**, and **12c** was assessed at two concentrations using the MV4-11 cell line, corresponding to their anti-proliferative IC_{50} values (5.85, 11.77, 0.29, and 0.34 μM), with comparisons to a control group. These compounds, which exhibited potent cytotoxicity, were chosen for further investigation of their effects on cell cycle progression. The results, presented in Table 4 and Fig. S84, reveal that compounds **12a** and **12c** notably reduced the percentage of cells in the G2/M phase (6.64% and 10.59%, respectively) compared to the control group (20.98%). Additionally, the percentage of cells in the subG1 phase increased by approximately 4- and 3-fold, relative to the control, indicating that these compounds induced cell arrest at the subG1 phase. At higher concentrations (1 μg mL^{-1}), compounds **12a** and **12c** caused an increase in cell death, as evidenced by a higher proportion of cells in the subG1 phase, reflecting an enhanced cytotoxic effect. In contrast, compound **7b** at 10 μg mL^{-1} caused a statistically significant ($p < 0.05$) increase in the S phase by 1.49-fold more than the control and a decrease in the G2/M phase but did not induce cell death, as indicated by the subG1 percentage (6.15 ± 2.74%). The subG1 checkpoint prevents the replication of damaged DNA, allowing repair and inhibiting the proliferation of damaged cells. Arrest at this phase indicates severe DNA damage, potentially triggering apoptosis. The sub G1 phase arrest induced by compounds **12a** and **12c** highlights their selectivity for CDK6, a key regulator of the G1 phase transition. Palbociclib was reported to induce a cell cycle arrest at the G1 phase in the MV4-11 cancer cell line.[43]

Enzymatic caspase-3/7 activity assay

Apoptosis is essential for controlling tumor growth and treatment efficacy. Many cancer therapies target this process by activating apoptotic pathways. A central mediator of apoptosis is *caspase-3*, a protein produced by the *CASP3* gene, which plays a pivotal role in executing programmed cell death.[44] In this study, compounds **6b**, **7b**, **12a**, and **12c** were tested. Based on the test results, hepatic cancer lines (HepG2) were selected as the targeted model due to their high sensitivity to the synthesized derivatives, as well as the presence of relevant caspases, such as caspase-3/7, and their expression of multiple metabolizing enzymes.[45] Evaluating the activity of the released caspase-3 is considered the most accurate method to examine the sound effects of the most active compounds **6b**, **7b**, **12a** and **12c** on the apoptotic role of caspase 3. The results presented in Table 5 and Fig. S85 reveal the capability of compound **7b** at a 5 μg mL^{-1} dose to elevate the activity of caspase-3/7 more than that of the control. Additionally, **6b**, **12a**, and **12c** did not increase caspase 3/7 activity, compared to the control. Among these compounds, **7b**, containing an adenine nucleus, induced apoptosis through the contribution of caspase-3/7 activity slightly more than those containing allopurinol. The results suggest that caspase activation is not a primary mechanism of action for most of the tested compounds.

Table 5 Relative caspase-3/7 activity compared with the control against HepG2 cells

Entry	Relative caspase-3/7 activity ± SD
Ctrl	1
6b, 5 μg mL^{-1}	0.982 ± 0.128
7b, 5 μg mL^{-1}	1.296 ± 0.190
12a, 5 μg mL^{-1}	0.840 ± 0.200
12c, 5 μg mL^{-1}	0.927 ± 0.185

In vitro CDK6 inhibitory assay

The most active towards cell proliferation compounds **6b**, **7b**, **8b** and **12a–12c** were screened owing to their potential inhibition of CDK6 enzyme using palbociclib as the reference drug, as shown in Table 6 and Fig. S86. Fortunately, all compounds proved to be potent inhibitors with pIC_{50} ranging from 5.82 ± 0.059 to 7.17 ± 0.003. Notably, compound **12a** exhibited pIC_{50},

Table 6 *In vitro* inhibitory activities of **6b**, **7b**, **8b**, **12a–c**, and **13b** against CDK6, VEGFR-2 and xanthine oxidase enzymes compared with palbociclib, sorafenib and allopurinol reference compounds, respectively

Entry	pIC_{50} CDK6 ± SD	pIC_{50} VEGFR-2 ± SD	pIC_{50} XO ± SD
6a	6.22 ± 0.023	6.51 ± 0.012	4.36 ± 0.55
7b	5.82 ± 0.059	6.29 ± 0.02	4.18 ± 0.82
8b	7.17 ± 0.003	7.15 ± 0.003	4.66 ± 0.33
12a	6.81 ± 0.006	7.27 ± 0.002	4.94 ± 0.16
12b	6.91 ± 0.048	6.92 ± 0.006	4.51 ± 0.62
12c	6.93 ± 0.005	6.84 ± 0.009	4.83 ± 0.23
13b	6.09 ± 0.032	6.49 ± 0.012	4.41 ± 0.49
Palbociclib	6.79 ± 0.006	—	—
Sorafenib	—	7.25 ± 0.002	—
Allopurinol	—	—	4.57 ± 0.13

matching the reference palbociclib (pIC_{50} 6.79 ± 0.006), while compounds **8b**, **12b** and **12c** showed a higher pIC_{50} range of 6.91 ± 0.048 to 7.17 ± 0.003. These results position these compounds as strong candidates for further exploration and development as potential therapeutic CDKI leads. The lowest CDK6 inhibition effect of compound **7b** has a pIC_{50} value of 5.82. In the studied series, the most active compounds **12a–12d** bind with the assigned fingerprint amino acids of the targeted active site. Furthermore, they bind with His100, which denotes selectivity for the CDK6 inhibitor. Overall, the ligand–protein binding pattern of **12a–12d** with some extra amino acids out of the fingerprint residues kept within the ATP pocket enhances the binding affinity to the target site, possibly enhancing their inhibitory efficacy.

In vitro VEGFR-2 inhibitory assay

The most potent antitumor derivatives **6b**, **7b**, **8b** and **12a–12c** were tested for VEGFR-2 kinase inhibition using sorafenib as the reference compound. The results of pIC_{50} values are presented in Table 6 and Fig. S86. Compounds **8b** and **12a** showed the most potent inhibition of VEGFR-2, achieving pIC_{50} values of 7.15 and 7.27, respectively, comparable to the standard inhibitor, sorafenib (pIC_{50} = 7.25).

The docking results revealed that the ethylene linker between the two heteroaromatic rings shared the same groove as the urea linker in sorafenib, contributing to a greater affinity for the VEGFR-2 enzyme. The formation of hydrogen bonds with Cys919, Asp1046, and Glu889, along with hydrophobic interactions, likely enhances the affinity of the heterocyclic pyrazolopyrimidine scaffold for the VEGFR-2 enzyme. In addition to the strong correlation between binding energies and pIC_{50} values, as described in eqn (1), Fig. 12 indicates that ligand binding is primarily driven by interactions with the protein. This relationship is expressed as follows:

$$\text{Binding energy} = -1.8467 \times pIC_{50} + 4.2391. \quad (1)$$

$$N = 7,\ r^2 = 0.91,\ p < 0.05$$

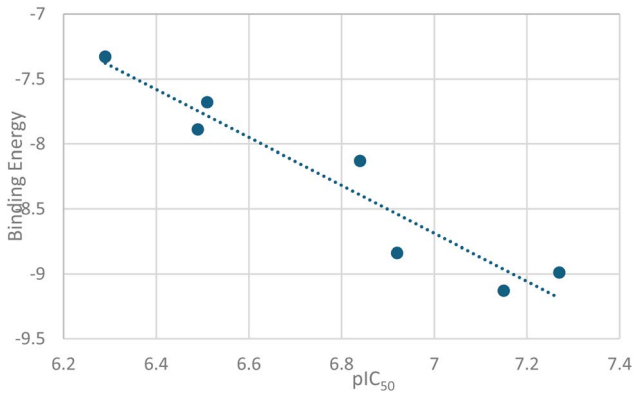

Fig. 12 Correlation between the calculated binding energy score Δ*G* and pIC_{50} for compounds **6b**, **7b**, **8b**, **12a–c** and **13b**.

Structure–activity relationship (SAR). Although a full SAR study is premature at this stage, initial observations reveal that the substituent pattern defined in Scheme 1 plays a pivotal role in modulating inhibitory activity. Compounds **6b**, **7b**, **8b**, **10b**, and **12b**, all of which carry a 5-chloro substituent, demonstrate significantly enhanced potency. This enhancement may be explained by chlorine's capacity to participate in specific non-covalent interactions, including hydrogen and halogen bonding, which contribute to tighter receptor binding. Structural modeling indicates that the chlorine atom in these compounds forms halogen bonds with the carbonyl oxygen of Val101 (3.01–3.26 Å), supported by bond angles (C–Cl···O) in the range of 170–174.9° and favorable Cl···O–C angles (111–121°). These features enable stable and directed interactions within the CDK6 active site. In compound **12b**, for example, the 5-chloro group facilitates binding to both His100 and Val101

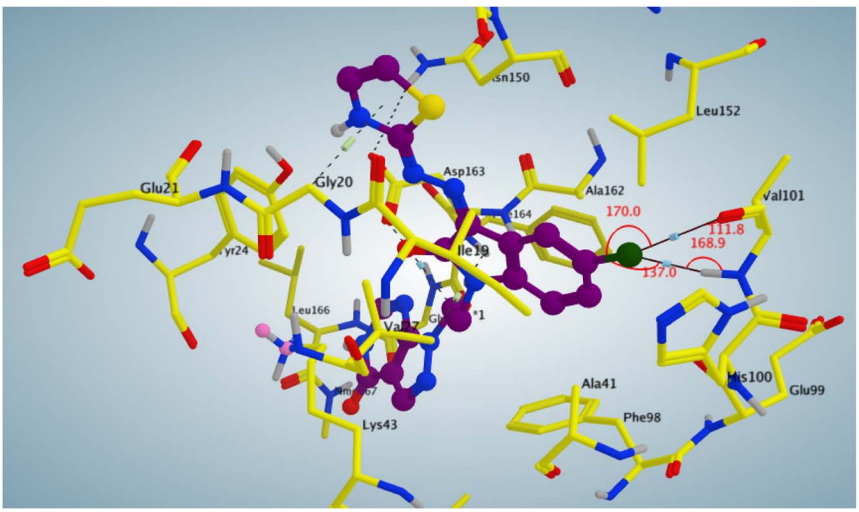

Fig. 13 Representative example of a halogen bond in compound **12b** with His100 and vicinal Val101 in the CDK6 active site.

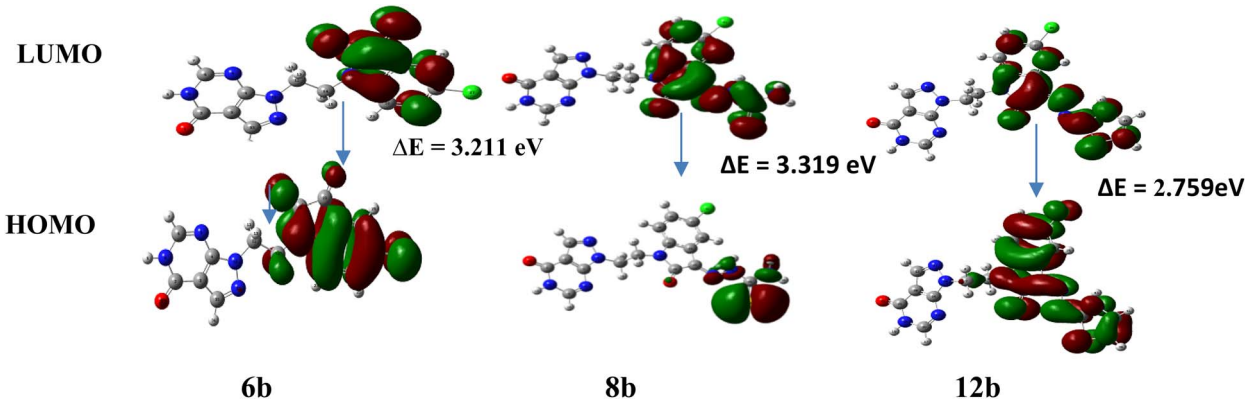

Fig. 14 Representative frontier molecular orbitals of compounds **6b**, **8b** and **12b**.

(Fig. 13), further enhancing receptor affinity. Moreover, compounds **12a–12d**, bearing a fused pyrazolopyrimidine and thiazole framework, exhibit an extended binding mode within the CDK6 pocket, which may account for their potent inhibitory effects.

Additionally, the predicted binding modes of compounds **8b** and **12b** within the CDK6 template structures were well-aligned, as shown in SI Fig. S87. These compounds demonstrated strong affinity for the ATP-binding site of CDK6, particularly interacting with Val101 and Asp163, with alignment scores of −126.70 and −116.67 kcal mol^{-1}, respectively.

Evaluation of xanthine oxidase inhibitory activity

The results of the *in vitro* XO inhibitory activity assay, as presented in Table 6 and Fig. S86, demonstrated that screened compounds **6b**, **7b**, **8b** and **12a–c** exhibited significant xanthine oxidase inhibitory activity with pIC_{50} values ranging from 4.18 ± 0.82 to 4.94 ± 0.16. Among this series, the most active compounds **12a** and **12c** against XO have pIC_{50} 4.94 and 4.83 distinct from allopurinol pIC_{50} 4.57, respectively.

Kinetics of xanthine oxidase (XO) inhibition. Enzyme inhibition can generally be categorized as competitive, uncompetitive, noncompetitive, or mixed.[46,47] The Lineweaver–Burk plot (Fig. S88) for compound **12a** displays intersecting lines to the left of the *y*-axis and above the *X*-axis, which is characteristic of mixed-type inhibition. This indicates that the inhibitor can bind both to the free enzyme and to the enzyme–substrate complex although with varying affinities.[48,49] Simultaneous increase in K_m and decrease in Vmax shown by **12a** and the reference allopurinol support the suggested mixed XOI mechanism. These conclusions are supported by strong correlation coefficients of 0.996 for **12a** and 0.958 for allopurinol (Table 7).

Table 7 Kinetic parameters of allopurinol and **12a** against xanthine oxidase in the enzyme kinetic study

	12a		Allopurinol	
Conc. (μM)	K_m	V_{max}	K_m	V_{max}
XO	40	2.25	40	2.21
0.1	75	1.66	50	1.51
1	112	1.38	64	1.33
10	123	0.98	51	0.55

2D-QSAR study

A 2D-Quantitative Structure–Activity Relationship (2D-QSAR) model was developed to predict the root for the perspective design of new ligands against HepG2 hepatocellular carcinoma. The synthesized compounds were divided into a training set of 16 compounds for model development and a test set of 3 derivatives reserved for external validation. Molecular descriptors were calculated using the MOE (Molecular Operating Environment) software and categorized into seven clusters: physical properties, subdivided surface areas, atom and bond counts, connectivity-based descriptors, partial charge descriptors, pharmacophore feature descriptors, and distance matrix descriptors.[50–52]

To identify the most significant structural predictors of activity, Stepwise Linear Regression Analysis (SLRA) was employed.[53] The QSAR model was developed using the Partial Least Squares (PLS) method with a dataset of 16 compounds. In accordance with QSAR modeling guidelines, the number of descriptors was limited to a maximum of three, ensuring a descriptor-to-compound ratio of approximately 1 : 5 to maintain model robustness and prevent overfitting.

The best QSAR model was selected based on its performance, which was evaluated using the highest correlation coefficient (R^2 = 0.90) and the lowest root mean square error (RMSE = 0.203), as shown in Fig. S89 and Table S2. The final model was a linear equation derived from using the Partial Least Squares (PLS) method and was based on three key molecular descriptors, as demonstrated in eqn (2):

$$pIC_{50} = 6.42560 + 0.10829 \times E_{vdW} - 0.00705 \times TPSA + 0.29934 \times \log P(o/w). \quad (2)$$

$$n = 16,\ RMSE = 0.20301,\ r^2 = 0.90112$$

The best-fit QSAR model revealed that the antiproliferative activity of the synthesized derivatives was influenced by three key molecular descriptors. van der Waals energy (E_{vdW}) exhibited a positive correlation with anticancer activity, as it plays a vital role in the formation of protein–ligand complexes. Similarly, lipophilicity ($\log P$(o/w)) is crucial for determining a compound's ability to penetrate hydrophobic barriers, such as cell membranes, to reach its site of action. However, the polar surface area (TPSA) showed an inverse correlation with the antiproliferative activity of the synthesized derivatives. TPSA reflects the ability of a ligand to form polar interactions, particularly hydrogen bonds, with specific biological targets. The Z-score method was used to identify outliers in the QSAR model, as presented in Table S2. In our study, none of the compounds had a Z-score above 2.5, indicating that all the compounds were consistent with the model predictions. This finding underscores the robustness and accuracy of the QSAR model. To validate the model, an independent test set comprising five compounds (**7b**, **9c**, and **12c**) was used for external validation. Additionally, two approved drugs, sunitinib and cisplatin, were included to strengthen the correlation and assess the model's predictive accuracy. The model's predictive performance was assessed by plotting the experimental pIC_{50} values against the predicted pIC_{50} values for these compounds. The model demonstrated a high predictive accuracy, with a correlation coefficient of $R^2 = 0.93$, as shown in Fig. S90. This strong correlation between the predicted and experimental values confirmed the model's robustness and reliability.

For the future development of novel compounds in this series, it is recommended to prioritize structural modifications that enhance E_{vdW} and $\log P$(o/w). This strategy is expected to improve the binding affinity of the compounds to biological targets, increase membrane permeability, and strengthen interactions.

In vitro chemical stability of compounds 6b, 8b, and 12a–12c

To assess the chemical stability of the most active compounds **6b**, **8b**, and **12a–12c** under simulated physiological conditions, each compound was incubated in phosphate buffer (pH 7.4) at 37 °C, and UV-Vis spectra were recorded over the 190–800 nm range at regular intervals up to 24 hours. The spectra remained consistent throughout the study, with no significant changes in absorbance intensity or the appearance of new peaks, indicating no degradation. These results support the chemical integrity of the compounds in buffered aqueous solutions, confirming their suitability for further biological studies. The full data are given in the SI, Fig. S91.

Determination of global reactivity descriptors

Density Functional Theory (DFT) calculations were conducted at the B3LYP level using the 6-31G basis set to investigate the structural characteristics of compounds **6b**, **7b**, **8b** and **12a–12c**, which exhibit the highest activity on the target enzyme CDK6. These calculations provided key insights into the molecular electronic structure through global reactivity descriptors. The descriptors include the energies of the highest occupied molecular orbital (HOMO) and lowest unoccupied molecular orbital (LUMO), as well as derived reactivity parameters, such as ionization potential (I), electron affinity (A), electronegativity (χ), chemical hardness (η), softness (s), chemical potential (μ), and electrophilicity (ω) (Table S3). These descriptors, particularly HOMO and LUMO energies, are critical for predicting the charge transfer, chemical reactivity, bioactivity, and stability of the compounds.[54–57] A higher HOMO energy suggests a stronger electron-donating ability and, therefore, greater chemical reactivity. In contrast, a lower LUMO energy indicates a higher electron-accepting capacity, also pointing to enhanced reactivity. In ligands **6b**, **8b** and **12a–12c**, HOMO electron density is primarily localized over the ethylene link and extended in the direction of the 5-Cl-oxindole and the thiazolylidene ring, indicating a propensity for electron donation during interactions with the CDK6 enzyme. The LUMO electron density, however, is distributed over the oxindole ring, as well as the sulfur and nitrogen atoms in the thiazolylidene ring, facilitating electron delocalization and influencing interactions with target molecules. Fig. 14 illustrates the orbital isosurface of the frontier molecular orbitals (HOMO and LUMO) of compounds **6b**, **8b** and **12b**, with positive phases depicted in green and negative phases in red. The energy gap (ΔE = LUMO − HOMO) serves as a key indicator of both chemical and biological activity; smaller energy gaps indicate higher reactivity and lower excitation energy requirements. In the studied series, the energy gap follows the trend: thiazolylidene derivatives **12a–12c** < thiosemicarbazone **8b** < unsubstituted compounds **6b** and **7b**. Among the 5-substituted oxindole derivatives, ΔE: 5-MeO < 5-Cl < 5-F < 5-H, signifying the increased reactivity of 5-substituted oxindole derivatives relative to their unsubstituted counterparts. Electrophilic and nucleophilic indices determine a molecule's ability to exchange electron density during reactions. The order of electron affinity, electronegativity, and chemical potential follows unsubstituted **6b**, **7b** > thiosemicarbazone **8b** > thiazolylidene derivatives **12a–12c**, indicating that thiazolylidene derivatives have the highest electron transfer capacity.

Molecular polarizability is linked to softness and hardness: "soft" molecules with lower hardness and higher softness are more polarized. Among the synthesized compounds, thiazolylidene derivatives **12a–12c**, with small energy gaps (ΔE = 2.558–2.800 eV), are classified as soft molecules, making them highly polarizable and biologically active. The electrophilicity index is essential for assessing a drug candidate's binding affinity to biological targets. Higher electrophilicity strengthens covalent interactions with nucleophilic residues in enzymes or receptor proteins, enhancing binding strength and specificity. Additionally, electron-withdrawing groups boost electrophilicity by stabilizing the LUMO, reducing the HOMO–LUMO energy gap, and increasing reactivity toward nucleophilic attack.

In conclusion, compounds **12b** and **12c**, which demonstrated the highest CDK6 inhibitory activity, exhibited a small energy gap and lower electrophilicity. These calculated descriptors provide valuable insights into drug design strategies, particularly in the optimization studies of these compounds.

Prediction of physicochemical properties of the most active compounds

The drug-likeness and molecular properties of the most active compounds, along with the reference drugs palbociclib and sorafenib, were evaluated using Molinspiration cheminformatics software[58] (Table S4). These parameters are essential for predicting the pharmacokinetics of the compounds, including their transport properties, reactivity, and metabolic stability within biological systems. All the targeted compounds, except for **10b** and **12c**, fully complied with Lipinski's Rule of Five. The number of rotatable bonds in the synthesized compounds was fewer than 10, indicating compliance with Veber's criteria[59] for molecular flexibility, suggesting that these compounds are likely to exhibit good oral bioavailability. Additionally, the TPSA values of the synthesized compounds ranged from 92.35 to 139.41 Å^2, further supporting their potential for oral bioavailability. Substituents at the C-5 position of the oxindole ring (–F, –Cl, and –OCH_3) increased the log *P* values and enhanced hydrophobicity and, consequently, the inhibitory potency against CDK6 through hydrophobic and van der Waals interactions. The most active compounds (**6b**, **8b**, and **12a–12d**) adhered to both Lipinski's and Veber's rules, highlighting their strong potential to inhibit the activities of CDK6, VEGFR-2, and xanthine oxidase.

Conclusion

This study presents a new class of oxindole derivatives derived from allopurinol and adenine, with promising multi-target anticancer potential. Compounds **6b**, **7b**, **8b**, and **12a–d** displayed potent cytotoxic effects, particularly toward HepG2 cells. Notably, allopurinol-derived hybrids (**12a–d**) showed enhanced activity over adenine-based analogs, attributable to chlorine-induced electronic effects. Mechanistic assays demonstrated pro-apoptotic activity (**12a** and **12c**), S-phase arrest (**7b**), and caspase activation. Enzymatic profiling and molecular modeling confirmed potent inhibition of CDK6, VEGFR-2, and xanthine oxidase, with key halogen/hydrogen bonding interactions at the CDK6 hinge region. The superior bioactivity of **12a–c** correlated with its soft electronic character. These findings position compounds **8b**, **12a**, and **12b** as compelling candidates for further development in anticancer therapeutics.

Experimental

Molecular docking study

The molecular docking simulation studies were performed on a Dell Precision T3600 workstation with Intel Xeon® CPU-1650.0 @ 3.20 GHz with a Windows 10 operating system using Molecular Operating Environment software (MOE 2020.01). The X-ray crystal structure of CDK6 co-crystalized with palbociclib (PDB ID: 5L2I) and Sorafenib with VEGFR-2 (PDB code 3WZE) was obtained from the protein data bank. Since the crystal structure contains a ligand molecule, the program automatically identifies the binding site, and we dock the tested ligands on it. Docking of the conformation database of the target ligands was done using the MOE-DOCK software wizard. To compare the conformers, London dG was used as a scoring function; lower values indicate more favorable poses. All the key interactions accomplished by the co-crystalized ligand with the key amino acids in the binding site are reproducible using the following docking setup.

Molecular dynamics simulation

The initial CDK6 complexes with palbociclib and compound **12b** were obtained *via* molecular docking. Molecular dynamics simulations (MDS) were conducted using NAMD 3.0 with the CHARMM27 force field.[60] Hydrogen atoms were added *via* the psfgen plugin in VMD 1.9. The systems were solvated in TIP3P water with 0.15 M Na^+ and Cl^- ions, energy minimized, heated to 300 K, and equilibrated for 1 ns. A 50 ns MDS was performed,[61] recording trajectory data every 0.1 ns to analyze RMSD, RMSF, hydrogen bonds, radius of gyration, and SASA. Ligand parameters were determined using CHARMM-GUI. Binding free energy was estimated *via* MM-PBSA using the fastDRH webserver with AmberTools 21, calculated as follows: $\Delta G_{\text{binding}} = G_{\text{complex}} - (G_{\text{receptor}} + G_{\text{inhibitor}})$. Each term involves calculating energy components, such as van der Waals, electrostatic, molecular mechanics, internal, and polar solvation energy.

Chemistry

Materials and methods. All the chemicals used for the synthesis of the target compounds were commercially available reagent grade and used without further purification, except the solvents, which were purified before use. *N*,*N*-Dimethylformamide (DMF) was purchased from Biochem and dried over molecular sieves (4 Å) prior to use. Isatin 98%, 5-chloroisatin 98%, and adenine 98% were obtained from Alfa Aesar Co., Germany. 5-Methoxyisatin 97% and 5-fluoroisatin 98% were obtained from Acros Organic Co., United Kingdom. Chemical reactions were monitored on thin layer chromatography (TLC) using precoated silica gel plates, 60 G F254, obtained from Merck, Darmstadt (Germany).

Silica gel (60–120 mesh) was used for column chromatography, and the developing systems used were: system (A): dichloromethane/methanol (9.5 : 0.5 v/v), system (B): chloroform/ethanol (9.7 : 0.3 v/v) and system (C): chloroform/ethyl acetate (2 : 1 v/v).

Melting points were measured using a Stuart® SMP10 melting point apparatus (Stuart Scientific, England) and were uncorrected. Infrared spectra (IR) were recorded using a Nicolet® iS10 FT-IR Spectrometer as KBr pellets at the Faculty of Science-Assiut University, Assiut, Egypt. The data are reported as the frequency of absorption (cm^{-1}). The NMR spectra were recorded using an AVANCE-III High Performance FT-NMR spectrometer, Brucker-Biospin International AG, Switzerland (400 MHz for ^{1}H and 100 MHz for ^{13}C) at the Faculty of Science-Zagazig University, Zagazig/Egypt. Chemical shifts are reported in parts per million (ppm, δ scale) using TMS as referenced relative to residual solvent DMSO-d6 (δ ^{1}H = 2.50, ^{13}C = 39.5

ppm). Coupling constants (J) for ^{1}H were reported in Hz, and spin multiplicities are represented by the following signals: singlet (s), doublet (d), triplet (t), doublet of doublet (dd) and multiplet (m). All raw fid files were processed, and the resulting spectra were analyzed using the program MestReNOVA 14.2 from Mestrelab Research S.L. Mass spectra (MS) were obtained using the inlet part to mass analyser in ThermoFisher scientific DPC-Direct Probe Controller model ISQ7000 single quadruple mass spectrometer at the Faculty of Science, Assiut University, Assiut, Egypt. Values are reported as the ratio of mass to charge in Daltons. The purity of the most active compounds **6b**, **8b**, **12a**, **12b** and **12c** is assessed by HPLC analysis at the Institute for Drug Development and Innovation Research, Assiut University, Assiut, Egypt.

General method for synthesis of 2-bromoethyl-substituted pyrazolopyrimidine and purine derivatives 3, 4

To a stirred suspension of allopurinol **1** or adenine **2** (1 mmol) and potassium carbonate (0.32 g, 2.3 mmol) in DMF (20 mL), 1,2-dibromoethane (0.75 g, 4 mmol) was added in a single portion. The mixture was stirred at room temperature for 24 h, after which the starting material was no longer detectable by TLC MeOH : DCM 1 : 9 and a new spot was detected. Then, the mixture was poured into crushed ice and left for 1 h. The precipitate was filtered, washed with cold water and dried at 80 °C.

1-(2-Bromoethyl)-1,5-dihydro-4*H*-pyrazolo[3,4-*d*]pyrimidin-4-one 3. Yield 2.0 g (82%), a pale-orange solid, mp 261–264 °C, recrystallized from ethanol. FT IR: 3435, 3083, 2969, 1694, 1582, 782, 695. ^{1}H NMR δ: 8.44–8.12 (m, 3H), 4.70–4.66 (t, J = 4 Hz, 2H), 4.37–4.28 (t, J = 4 Hz, 1H), 3.93–3.91 (t, J = 4 Hz, 1H). Mass spectrum = 242.02 (M. wt: 243.06).

9-(2-Bromoethyl)-9*H*-purin-6-amine 4. Yield 1.75 g (72%), an orange solid, mp: 295–298 °C (297–298 lit.[62]), washed with water. IR: 3362, 3323, 3150, 1652, 1599, 1385, 1325, 1309, 1246, 1074, 796, 708, 647. ^{1}H NMR δ: 8.19 (s, 1H), 8.15 (s, 1H), 7.27 (s, 2H), 4.57 (t, J = 5.97, 2H), 3.95 (t, J = 5.97, 2H).

General method for the synthesis of 1,5-disubstitutedindole-2,3-dione 6a–d and 7a–d

To a stirred solution of 5-(un) substituted-1*H*-indole-2,3-dione **5a–d** (4 mmol) and anhydrous potassium carbonate (0.83 g, 6 mmol) in dry DMF (5 mL), compounds **3** and **4** (4 mmol) were added. The reaction mixture was stirred at 60 °C for 6–8 h. The reaction mixture was then cooled to room temperature, poured into crushed ice and left for 1 h. The products were separated by filtration, dried and purified by column chromatography on a silica gel column using developing systems (A) as the mobile phase.

1-[2-(1,5-Dihydro-4-oxopyrazolo[3,4-*d*]pyrimidin-1-yl) ethyl] indole-2, 3-dione 6a. Yield 1.35 (88%), orange powder, reaction time 6 h, mp: 223–225 °C. IR: 3435, 3084, 2952, 1745, 1694, 1608, 1582, 1473. ^{1}H NMR δ: 8.33–8.00 (m, 3H), 7.55 (dd, J = 13.1, 6.9 Hz, 2H), 7.09 (dd, J = 14.9, 7.0 Hz, 1H), 6.87 (d, J = 7.9 Hz, 1H), 4.55 (s, 2H), 4.19–4.08 (m, 2H). ^{13}C NMR δ: 183.0, 158.3, 156.5, 151.8, 150.4, 150.1, 138.1, 135.0, 128.1, 124.5, 123.2, 110.3, 105.0, 44.3, 43.3. Elemental analyses found: C%, 58.43; H%, 3.77; N%, 22.91. Calc. for $C_{15}H_{11}N_5O_3$: C%, 58.25; H%, 3.58; O%, 22.64.

5-Chloro-1-[2-(1,5-dihydro-4-oxopyrazolo[3,4-*d*]pyrimidin-1-yl)ethyl]indole-2, 3-dione 6b. Yield 1.2 (70%), pale orange powder, reaction time 6.5 h, mp: 214–215 °C. IR: 3467, 3084, 2953, 1745, 1694, 1610, 1584, 1473. ^{1}H NMR δ: 8.11–7.97 (m, 3H), 7.60 (d, J = 7.4 Hz, 1H), 7.56 (d, J = 2.3 Hz, 1H), 6.92 (d, J = 8.0 Hz, 1H), 4.60–4.53 (m, 2H), 4.34–4.23 (m, 2H). ^{13}C NMR δ: 181.9, 157.8, 156.5, 151.6, 150.7, 148.6, 137.1, 136.0, 127.4, 124.0, 118.4, 111.9, 105.0, 44.3, 42.8. Elemental analyses found: C%, 52.67; H%, 3.05; N%, 20.63. Calc. for $C_{15}H_{10}ClN_5O_3$: C%, 52.41; H%, 2.93; N%, 20.37.

1-[2-(1,5-Dihydro-4-oxopyrazolo[3,4-*d*]pyrimidin-1-yl)ethyl]5-methoxyindole-2,3-dione 6c. Yield 1.2 g (71%), reddish orange powder, reaction time 7 h, mp: 226–228 °C. IR: 3458, 3084, 2945, 1736, 1697, 1621, 1598, 1490. ^{1}H NMR δ: 8.10–7.96 (m, 3H), 7.11 (d, 1H), 7.09 (d, J = 18.6 Hz, 2H), 6.79 (s, 1H), 4.64–4.27 (m, 2H), 4.27–4.03 (s, 1H), 4.03–3.90 (m, 1H), 3.73 (s, 3H). ^{13}C NMR δ: 183.2, 158.1, 156.5, 155.6, 151.6, 150.8, 144.2, 135.0, 124.0, 117.7, 111.1, 109.2, 105.0, 55.8, 44.3, 43.2. Elemental analyses found: C%, 56.82; H%, 4.03; N%, 20.89. Calc. for $C_{16}H_{13}N_5O_4$: C, % 56.64; H%, 3.86; N%, 20.64.

5-Fluoro-1-[(2-(1,5-dihydro-4-oxopyrazolo[3,4-*d*]pyrimidin-1-yl)ethyl)]indole-2,3-dione 6d. Yield 1 g (63%), pale orange powder, reaction time 6.5 h, mp 219–220 °C, IR: 3450, 3056, 2952, 1741, 1697, 1624, 1583,1486. ^{1}H NMR δ: 8.35–8.01 (m, 2H),7.46 (s, 2H), 6.93 (s, 1H), 4.54 (s, 2H), 4.22–4.09 (m, 2H). ^{13}C NMR δ: 182.8, 160.1, 158.5, 157.6, 156.9, 152, 147.1, 136.9, 135.4, 128.5, 124.5, 112.0, 105.4, 44.7, 43.9. Elemental analyses found: C%, 55.31; H%, 3.20; N%, 21.67. Calc. for $C_{15}H_{10}FN_5O_3$: C%, 55.05; H%, 3.08; N%, 21.40.

1-[2-(6-Amino-9*H*-purin-9-yl)ethyl]-2,3-dihydro-1*H*-indole-2,3-dione 7a. Yield 1.4 g (91%), orange powder, reaction time 8 h, mp: 244–246 °C (decomp.), (lit. 242 °C).[62] IR: 3441, 3317, 3157, 3103, 2940, 1740, 1651, 1610, 1596, 1473. ^{1}H NMR δ: 8.16 (s, 1H), 7.95 (s, 1H), 7.65–7.38 (m, 2H), 7.16 (s, 2H), 7.04 (t, J = 7.5 Hz, 1H), 6.89 (d, J = 7.9 Hz, 1H), 4.44 (t, J = 5.3 Hz, 2H), 4.11 (t, J = 5.3 Hz, 2H). ^{13}C NMR δ: 183.3, 158.7, 156.2, 152.7, 150.7, 150.1, 141.3, 138.2, 124.7, 123.5,119, 117.8, 110.3, 41.1, 40.3. Mass spectrum: m/z 308.26 $[M]^+$; M. wt: 308.29. Elemental analyses found: C%, 58.67; H%, 4.08; N%, 27.49. Calc. for $C_{15}H_{12}N_6O_2$: C%, 58.44; H%, 3.92; N%, 27.26.

1-[2-(6-Amino-9*H*-purin-9-yl)ethyl]-5-chloro-2,3-dihydro-1*H*-indole-2,3-dione 7b. Yield 1.5 g (87.5%), pale orange powder, reaction time 7.5 h, mp: 259–261 °C. IR: 3441, 3320, 3174, 3031, 1740, 1654, 1605, 1577, 1477. ^{1}H NMR δ: 8.15 (s, 1H), 7.93 (s, 1H), 7.62–7.48 (m, 2H), 7.16 (s, 2H), 6.93 (d, J = 8.3 Hz, 1H), 4.41 (s, 2H), 4.11 (d, J = 4.7 Hz, 1H). ^{13}C NMR δ: 181.9, 159.2, 158, 155.8, 152.4, 148.8, 140.9, 136.7, 127.2, 123.7, 118.6, 113.8, 111.6, 42.7, 40.6. Elemental analyses found: C%, 52.73; H%, 3.42; N%, 24.68. Calc. for $C_{15}H_{11}ClN_6O_2$: C, 52.56; H, 3.23; N, 24.52.

1-[2-(6-Amino-9*H*-purin-9-yl)ethyl]-2,3-dihydro-5-methoxy-1*H*-indole-2,3-dione 7c. Yield 1.2 g (71%), reddish orange powder, reaction time 6 h, mp: 260–264 °C. IR: 3365, 3308, 3143, 2963, 1740, 1667, 1600, 1576, 1492. ^{1}H NMR δ: 8.14 (s, 1H), 7.96

(s, 1H), 7.15 (s, 2H), 7.05 (d, J = 8.1 Hz, 2H), 6.84 (d, J = 7.3 Hz, 1H) 4.41 (s, 2H), 4.07 (s, 2H), 3.72 (s, 3H). ^{13}C NMR δ: 179.1, 161.3, 156.2, 152.7, 150.1, 141.3, 136.7, 131.5, 120.7, 119, 117, 110.4, 106.6, 56.0, 41.3, 40.5. Elemental analyses found: C%, 56.88; H%, 4.35; N%, 24.99. Calc. for $C_{16}H_{14}N_6O_3$: C%, 56.80; H%, 4.17; N%, 24.84.

1-[2-(6-Amino-9*H*-purin-9-yl)ethyl]-2,3-dihydro-5-fluoro-1*H*-indole-2,3-dione 7d. Yield 1.45 g (92%), pale orange powder, reaction time 6.5 h, mp: 230–233 °C. IR: 3368, 3325, 3159, 3103, 1739, 1652, 1603, 1577, 1485. ^{1}H NMR δ: 8.15 (s, 1H), 7.93 (s, 1H), 7.36 (d, J = 7.0 Hz, 2H), 7.16 (s, 2H), 6.93 (d, J = 5.5 Hz, 1H), 4.44 (t, J = 5.3, 2H), 4.10 (t, J = 5.3, 2H). ^{13}C NMR δ: 182.9, 159.9, 158.7, 157.5, 156.2, 152.8, 150.1, 146.9, 141.4, 124.3, 124.1, 118.9, 111.6, 43.0, 41.1. Elemental analyses found: C%, 55.41; H%, 3.57; N%, 26.04. Calc. for $C_{15}H_{11}FN_6O_2$: C%, 55.22; H%, 3.40; N%, 25.76.

General method of synthesis of oxindole-3-thiosemicarbazone derivatives 8a–d–9a–d

The appropriate isatin derivative **6a–d**, **7a–d** (1 mmol) and thiosemicarbazide (0.09 g, 1 mmol) were dissolved in warm ethanol (20 mL). The reaction mixture was acidified by the addition of few drops of glacial acetic acid and refluxed for 2–4 h. The mixture was cooled to room temperature, and the separated precipitate was filtrated, washed with ethanol, and dried. The product was purified by recrystallization from ethanol.

(2*Z*)-2-{2-Oxo-1-[2-(4-oxo-1,5-dihydrpyrazolo[3,4-*d*]pyrimidin-1-yl)ethyl]-1,2-dihydro-3*H*-indol-3-ylidene}hydrazine-1-carbothioamide 8a. Yield 0.28 g (75%), yellow powder, reaction time 2 h, mp 245–248 °C. IR: 3420, 3260, 3163, 3083, 2951, 1694, 1612, 1358, 782. ^{1}H NMR δ: 12.22 (s, 1H), 9.09 (s, 1H), 8.72 (s, 1H), 8.26–7.96 (m, 2H), 7.67–7.62 (t, J = 8 Hz, 1H), 7.30–7.26 (m, J = 8 Hz, 1H), 7.08 (d, J = 6.8 Hz, 1H), 6.79 (dd, J = 8, 7.5 Hz, 1H), 4.65 (s, 2H), 4.30–4.07 (m, 2H). ^{13}C NMR δ: 179.4, 162.8, 161.2, 156.7, 152.1, 151.1, 142.7, 135.4, 131.4, 123.1, 121.1, 119.7, 109.8, 105.7, 44.7, 43. Elemental analyses, found: C%, 50.49; H%, 3.80; N%, 29.47; S%, 8.46. Calc. for $C_{16}H_{14}N_8O_2S$: C%, 50.25; H%, 3.69; N%, 29.30; S%, 8.39.

(2*Z*)-2-{5-Chloro-2-oxo-1-[2-(4-oxo-1,5-dihydropyrazolo[3,4-*d*]pyrimidin-1-yl)ethyl]-1,2-dihydro-3*H*-indol-3-ylidene}hydrazine-1-carbothioamide 8b. Yield 0.3 g (70%), yellow powder, reaction time 2.5 h, mp: 250–252 °C. IR: 3431, 3265, 3172, 3056, 2928, 1694, 1597, 1348, 782. ^{1}H NMR δ: 12.07 (s, 1H), 9.18 (s, 1H), 8.85 (s, 1H), 8.27–7.98 (m, 3H), 7.77 (d, J = 16.5 Hz, 1H), 7.36 (s, 1H), 6.84 (d, J = 14.8 Hz, 1H), 4.58 (s, 2H), 4.29–4.14 (m, 2H). ^{13}C NMR δ: 178.7, 160.5, 156.4, 151.5, 150.6, 140.9, 135.0, 130.1, 129.3, 127.1, 121.0, 120.3, 110.7, 105.0, 45.3, 44.5. Elemental analyses found: C%, 46.32; H%, 3.40; N%, 27.15; S%, 7.78. Calc. for $C_{16}H_{13}ClN_8O_2S$: C%, 46.10; H%, 3.14; N%, 26.88; S%, 7.69.

(2*Z*)-2-{5-Methoxy-2-oxo-1-[2-(4-oxo-1,5-dihydropyrazolo[3,4-*d*]pyrimidin-1-yl)ethyl]-1,2-dihydro-3*H*-indol-3-ylidene} hydrazine-1-carbothioamide 8c. Yield 0.25 g 68.5%, pale orange powder, reaction time 4 h, mp: 252–253 °C. IR: 3429, 3265–3168, 3056, 2943, 1693, 1596, 1357, 782. ^{1}H NMR δ: 12.16 (s, 1H), 9.09 (s, 1H), 8.75 (s, 1H), 8.21–7.99 (m, 3H), 7.37 (d, J = 14.4 Hz, 1H), 7.04–6.73 (m, 2H), 4.53 (s, 2H), 4.29–4.14 (m, 2H), 3.73 (s, 3H). ^{13}C NMR δ: 179.2, 160.8, 156.4, 155.6, 151.6, 150.6, 136.1, 134.9, 130.9, 120.1, 116.8, 110.1, 106.3, 105.0, 55.6, 44, 43.7. Elemental analyses found: C%, 49.78; H%, 4.05; N%, 27.30; S%, 7.91. Calc. for $C_{17}H_{16}N_8O_3S$: C%, 49.51; H%, 3.91; N%, 27.17; S%, 7.77.

(2*Z*)-2-{5-Fluoro-2-oxo-1-[2-(4-oxo-1,5-dihydropyrazolo[3,4-*d*]pyrimidin-1-yl)ethyl]-1,2-dihydro-3*H*-indol-3-ylidene}hydrazine-1-carbothioamide 8d. Yield 0.3 g (82%), yellow powder, reaction time 2.5 h, mp 230–233 °C. IR: 3430, 3268, 3168, 3056, 2952, 1694, 1583, 1352, 782. ^{1}H NMR δ: 12.09 (s, 1H), 9.18 (s, 1H), 8.83 (s, 1H), 8.28–8 (m, 3H), 7.53 (s, 1H), 7.16 (s, 1H), 6.84 (d, J = 17.7 Hz, 1H), 4.55 (s, 2H), 4.35–4.13 (m, 2H). ^{13}C NMR δ: 180.1, 161.2, 157.7, 156.9, 152.1, 151.1, 139.0, 135.6, 130.4, 121.3, 117.6, 110.9, 108.2, 105.0, 44.9, 43.2. Elemental analyses found: C%, 48.23; H%, 3.45; N%, 28.17; S%, 8.14. Calc. for $C_{16}H_{13}FN_8O_2S$: C%, 48.00; H%, 3.27; N%, 27.99; S%, 8.01.

(2*Z*)-2-{2-Oxo-1-[2-(6-aminopurine-9-yl)ethyl]-1,2-dihydro-3*H*-indol-3-ylidene}hydrazine-1-carbothioamide 9a. Yield 0.35 g (94%), bright yellow powder, reaction time 2.5 h, mp: 276–277 °C, IR: 3373, 3312, 3265, 3170, 2931, 1677, 1600, 1304, 1172. ^{1}H NMR δ: 12.26 (s, 1H), 9.10 (s, 1H), 8.74 (s, 1H), 8.10 (s, 1H), 8.00 (s, 1H), 7.63 (d, J = 7.3 Hz, 1H), 7.24 (t, J = 7.4 Hz, 1H), 7.16 (s, 2H), 7.06 (t, J = 7.4 Hz, 1H), 6.82 (d, J = 7.8 Hz, 1H), 4.46 (t, J = 5.5 Hz, 2H), 4.18 (t, J = 5.5 Hz, 2H). ^{13}C NMR δ: 179.1, 161.4, 156.2, 152.8, 150.1, 143.0, 141.2, 131.4, 131.3, 123.2, 121.1, 119.8, 119.1, 109.5, 41.3, 40.3. Elemental analyses found: C%, 50.52; H%, 4.17; N%, 33.19; S%, 8.53. Calc. for $C_{16}H_{15}N_9OS$: C%, 50.38; H%, 3.96; N%, 33.05; S%, 8.41.

(2*Z*)-2-{5-Chloro-2-oxo-1-[2-(6-aminopurine-9-yl)ethyl]-1,2-dihydro-3*H*-indol-3-ylidene}hydrazine-1-carbothioamide 9b. Yield 0.4 g (94%), yellow powder, reaction time 3.5 h, mp 281–283 °C. IR: 3450, 3248, 3289, 3248, 3110, 2951, 1697, 1610, 1303, 1170. ^{1}H NMR δ: 12.07 (s, 1H), 9.15 (s, 1H), 8.84 (s, 1H), 8.09 (s, 1H), 7.98 (s, 1H), 7.72 (d, J = 2.2 Hz, 1H), 7.29 (dd, J = 8.5, 2.2 Hz, 1H), 7.14 (s, 2H), 6.84 (d, J = 8.5 Hz, 1H), 4.44 (t, J = 5.5 Hz, 2H), 4.17 (t, J = 5.5 Hz). ^{13}C NMR δ: 178.7, 160.6, 155.8, 152.3, 149.6, 141.2, 140.8, 140.4, 129.9, 126.9, 121.1, 120.3, 118.5, 110.6, 42.6, 40.8. Elemental analyses found: C%, 46.34; H%, 3.48; N%, 30.17; S%, 7.84. Calc. for $C_{16}H_{14}ClN_9OS$: C%, 46.21; H%, 3.39; N%, 30.31; S%, 7.71.

(2*Z*)-2-{5-Methoxy-2-oxo-1-[2-(6-aminopurine-9-yl)ethyl]-1,2-dihydro-3*H*-indol-3-ylidene} hydrazine-1-carbothioamide 9c. Yield 0.3 g (82%), yellowish orange powder, and reaction time 4 h, mp 244–245 °C. IR: 3446, 3294, 3244, 3142, 2927, 1694, 1603, 1304, 1164. ^{1}H NMR δ: 12.19 (s, 1H), 9.08 (s, 1H), 8.74 (s, 1H), 8.06 (s, 1H), 8.01 (s, 1H), 7.29 (s, 1H), 7.13 (s, 2H), 6.80–6.74 (m, 2H), 4.43 (s, 2H), 4.13 (s, 2H), 3.72 (s, 3H). ^{13}C NMR δ: 178.7, 160.9, 155.8, 155.6, 152.3, 149.7, 140.8, 136.3, 131.1, 120.16, 118.6, 116.6, 109.9, 106.2, 55.6, 42.6, 40.8. Elemental analyses found: C%, 49.89; H%, 4.30; N%, 30.82; S%, 7.90. Calc. for $C_{17}H_{17}N_9O_2S$: C%, 49.63; H%, 4.16; N%, 30.64; S%, 7.79.

(2*Z*)-2-{5-Fluoro-2-oxo-1-[2-(6-aminopurine-9-yl)ethyl]-1,2-dihydro-3*H*-indol-3-ylidene}hydrazine-1-carbothioamide 9d. Yield 0.35 g (95%), yellow powder, reaction time 3 h, mp 279–281 °C. IR: 3420, 3362, 3321, 3150, 2951, 1652, 1599, 1309, 1174; ^{1}H NMR δ: 12.12 (s, 1H), 9.15 (s, 1H), 8.78 (s, 1H,), 8.08 (s, 1H), 7.97 (s, 1H), 7.45 (d, J = 5.3 Hz, 1H), 7.14 (s, 2H), 7.08 (d, J =

8.1 Hz, 1H), 6.82 (s, 1H), 4.44 (s, 2H), 4.16 (s, 2H). ^{13}C NMR δ: 178.8, 161.0, 157.3, 155.8, 152.4, 149.7, 140.9, 138.9, 130.4, 120.8, 118.5, 116.9, 110.3, 107.9, 40.9, 40.1. Elemental analyses found: C%, 48.27; H%, 3.49; N%, 31.75; S%, 8.11. Calc. for $C_{16}H_{14}FN_9OS$: C%, 48.11; H%, 3.53; N%, 31.56; S%, 8.03.

Synthesis of 1,5-disubstituted-(3*Z*)-3-[(2*E*/*Z*)-(4-oxo-1,3-thiazolidin-2-ylidene)hydrazinylidene]-1,3-dihydro-2*H*-indol-2-one 10a–d and 11a–d

A mixture of appropriate 2-substituted hydrazine-1-carbothioamides series **8a–d**, **9a–d** (1 mmol), ethyl bromoacetate for **8a–d** or monochloroacetic acid for **9a–d** (0.17 g, 1 mmol) and anhydrous sodium acetate (0.16 g, 2 mmol) in ethanol (50 ml) were refluxed for 24 h, the reaction mixture was cooled, poured into crushed ice. The formed precipitate was filtered, dried, and purified by silica gel column using the developing system (B) for compounds **10a–d** and (C) for **11a–d**.

1-[2-(4-Oxo-1,5-dihydro-4*H*-pyrazolo[3,4-*d*]pyrimidine-1-yl) ethyl]-(3*Z*)-3-[(2*E*/*Z*)-(4-oxo-1,3-thiazolidin-2-ylidene)hydrazinylidene]-1,3-dihydro-2*H*-indol-2-one 10a. Yield 0.3 g (68%), orange powder, mp: 265–267 °C, IR: 3435, 3050, 2954, 1744, 1697, 1597, 1351, 783. ^{1}H NMR δ: 12.23 (s, 1H), 8.24–7.97 (m, 3H), 7.49 (dd, J = 13.6, 7.3 Hz, 1H), 7.30 (d, J = 7.1 Hz, 1H), 7.00 (d, J = 6.6 Hz, 2H), 6.87–6.61 (m, 1H), 4.55 (s, 2H), 4.19 (d, J = 7.8 Hz, 3H) 3.97 (s, 2H). ^{13}C NMR δ: 171.8, 166.4, 156.9, 156.3,151.5, 150.4, 145.9, 134.8, 132.3, 130, 122.2, 121.2, 119.5, 108.7, 104.9, 48, 44.6, 32.2. Mass spectrum: m/z $[M]^+$ = 422.42; found 422.21. Elemental analyses found: C%, 51.42; H%, 3.52; N%, 26.80; S%, 7.71. Calc. for $C_{16}H_{13}FN_8O_2S$: C%, 51.18; H%, 3.34; N%, 26.53; S%, 7.59.

5-Chloro-1-[2-(4-Oxo-1,5-dihydro-4*H* pyrazolo[3,4-*d*] pyrimidine-1-yl) ethyl]-(3*Z*)-3-[(2*E*/*Z*)-(4-oxo-1,3-thiazolidin-2-ylidene) hydrazinylidene]-1,3-dihydro-2*H*-indol-2-one 10b. Yield 0.27 g (61.5%), reddish orange powder, mp: 288–290 °C dec., IR: 3435, 3084, 2952, 1694 (2C=O), 1582, 1374, 783. ^{1}H NMR δ: 12.06 (s, 1H), 8.26–7.97 (m, 3H), 7.74–7.34 (m, 2H), 6.80–6.70 (m, 1H), 4.53 (s, 2H), 4.21–4.07 (m, 2H), 3.94 (s, 2H). ^{13}C NMR δ: 171.9, 166.7, 163.0, 158.4, 157.8, 156.6, 151.8, 150.75, 149.6, 145.0, 135.1, 130.2, 126.4, 106.0, 104.9, 45.4, 44.6, 31.2. Elemental analyses found: C%, 47.59; H%, 3.05; N%, 24.71; S%, 7.14. Calc. for $C_{18}H_{13}ClN_8O_3S$: C%, 47.32; H%, 2.87; N%, 24.53; S%, 7.02.

5-Methoxy-1-[2-(4-oxo-1,5-dihydro-4*H*-pyrazolo[3,4-*d*]pyrimidine-1-yl)ethyl]-(3*Z*)-3-[(2*E*/*Z*)-(4-oxo-1,3-thiazolidin-2-ylidene) hydrazinylidene]-1,3-dihydro-2*H*-indol-2-one 10c. Yield 0.25 g (57%), orange powder, mp 290–291 °C dec., IR: 3446, br., 3084, 2952, 1696, 1596, 1352, 783. ^{1}H NMR δ: 12.58 (s, 1H), 8.50–7.97 (m, 3H), 7.00–6.63 (m, 3H), 466–4.50 (m, 2H), 4.19 (s, 2H), 3.94 (s, 2H), 3.74 (s, 3H). ^{13}C NMR δ: 171.8, 166.7, 158.4, 157.8, 157.1, 156.4, 155.1, 151.5, 150.5, 135.0, 130.1, 118.0, 109.3, 106.0, 105.0, 55.6, 44.5, 43.7, 32.3. Elemental analyses found: C%, 50.67; H%, 3.62; N%, 24.85; S%, 7.18. Calc. for $C_{19}H_{16}N_8O_4S$: C%, 50.44; H%, 3.56; N%, 24.77; S%, 7.09.

5-Fluoro-1-[2-(4-oxo-1,5-dihydro-4*H*-pyrazolo[3,4-*d*]pyrimidine-1-yl)ethyl]-(3*Z*)-3-[(2*E*/*Z*)-(4-oxo-1,3-thiazolidin-2-ylidene) hydrazinylidene]-1,3-dihydro-2*H*-indol-2-one 10d. Yield 0.3 g (68%), orange powder, mp: 256–257 °C dec., IR: 3467, 3084, 2952, 1698. ^{1}H NMR δ: 12.75 (s, 1H), 8.50–7.98 (m, 3H), 7.74–6.62 (m, 3H), 4.51 (s, 2H), 4.21–3.96 (m, 4H). ^{13}C NMR δ: 171.8, 166.7, 157.0, 156.4, 151.5, 150.5, 147.4, 145.5, 134.9, 128.0, 116.6, 114.9, 110.2, 105.0, 44.5, 43.6, 32.6. Elemental analyses found: C%, 49.31; H%, 3.17; N%, 25.30; S%, 7.42. Calc. for $C_{18}H_{13}FN_8O_3S$: C%, 49.09; H%, 2.98; N%, 25.44; S%, 7.28.

1-[2-(6-Amino purine-9-yl)ethyl]-(3*Z*)-3-[(2*E*/*Z*)-(4-oxo-1,3-thiazolidin-2-ylidene) hydrazinylidene]-1,3-dihydro-2*H*-indol-2-one 11a. Yield 0.25 g (65%), dark yellow powder, mp: 302 °C dec., IR: 3366, 3188, 3067, 2983, 1698, 1613, 1541, 1337. ^{1}H NMR δ: 12.53 (s, 1H), 8.07 (s, 1H), 8.01 (s, 1H), 7.47 (d, J = 7.4 Hz, 1H), 7.28 (t, J = 8 Hz, 1H), 7.20 (s, 2H), 7.01 (t, J = 7.5 Hz, 1H), 6.81 (d, J = 7.6 Hz, 1H), 4.42 (t, J = 4 Hz, 2H), 4.12 (t, J = 4 Hz, 2H), 3.95 (s, 2H). ^{13}C NMR δ: 172.1, 163.5, 155.5, 155.2, 152.3, 151.9, 140.9, 134.9, 132.3, 131.8, 129.4, 128.2, 122.3, 118.5, 108.5, 42.2, 41.8, 33.3. Elemental analyses found: C%, 51.47; H%, 3.65; N%, 30.14; S%, 7.69. Calc. for $C_{18}H_{15}N_9O_2S$: C%, 51.30; H%, 29.91; S%, 7.61.

1-[2-(6-Amino purine-9-yl) ethyl]-5-chloro-(3*Z*)-3-[(2*E*/*Z*)-(4-oxo-1,3-thiazolidin-2-ylidene)hydrazinylidene]-1,3-dihydro-2*H*-indol-2-one 11b. Yield 0.28 g (64%), yellowish green powder, mp: 285 °C dec (decomp.), IR: 3429, 3232, 3079, 2927, 1705, 1622, 1540, 1334. ^{1}H NMR δ: 12.64 (br. s, 1H), 8.08 (s, 1H), 7.97 (s, 1H), 7.40 (d, J = 1.3 Hz, 1H), 7.33 (dd, J = 4.6, 2.4 Hz, 1H), 7.15 (s, 2H), 6.85 (t, J = 8 Hz, 1H), 4.42 (d, J = 4.7 Hz, 2H), 4.12 (t, J = 5.2 Hz, 2H), 4.03 (s, 2H). ^{13}C NMR δ: 174.5, 163.7, 156.1, 153, 152.6, 150.1, 146.1, 143.2, 141.3, 131.8, 128, 126.7, 119.0, 118.1, 110.4, 41.9, 41.2, 34.2. Elemental analyses found: C%, 47.60; H%, 3.24; N%, 27.88; S%, 7.12. Calc. for $C_{18}H_{14}ClN_9O_2S$: C%, 47.42; H%, 3.10; N%, 27.65; S%, 7.03.

1-[2-(6-Amino purine-9-yl) ethyl]-5-methoxy-(3*Z*)-3-[(2*E*/*Z*)-(4-oxo-1,3-thiazolidin-2-ylidene) hydrazinylidene]-1,3-dihydro-2*H*-indol-2-one 11c. Yield 0.25 g (57%), dark orange powder, mp: 290 °C, IR: 3362, 3145, 3070, 2928, 1701, 1600, 1541, 1337. ^{1}H NMR δ. 12.58 (s, 1H), 8.50–7.97 (m, 3H), 7.00–6.63 (m, 3H), 4.43 (s, 2H), 4.26 (s, 2H), 4.13 (s, 2H), 3.74 (s, 3H). ^{13}C NMR δ: 71.8, 166.7, 156.4, 155.1, 151.5, 150.5, 146.3, 144.1, 135.0, 130.1, 125.3, 120.6, 119.2, 118.0, 109.3, 55.6, 44.5, 43.7, 33.1. Elemental analyses found: C%, 50.74; H%, 3.97; N%, 27.78; S%, 7.21. Calc. for $C_{19}H_{17}N_9O_3S$: C%, 50.55; H%, 3.80; N%, 27.92; S%, 7.10.

1-[2-(6-Amino purine-9-yl) ethyl]-5-fluoro-(3*Z*)-3-[(2*E*/*Z*)-(4-oxo-1,3-thiazolidin-2-ylidene) hydrazinylidene]-1,3-dihydro-2*H*-indol-2-one 11d. Yield 0.3 g (68%), dark yellow powder, mp: 298–299 °C, IR: 3378, 3336, 3072, 2926, 1705, 1631, 1543, 1336. ^{1}H NMR δ: 12.66 (s, 1H), 8.06 (s, 1H), 7.97 (s, 1H), 7.22 (d, J = 6.2 Hz, 1H,), 7.13 (s, 3H), 6.84 (d, J = 3.3 Hz, 1H), 4.40 (t, J = 4 Hz, 2H), 4.11 (t, J = 4 Hz, 2H), 3.96 (s, 2H). ^{13}C NMR δ: 174.6, 165.8, 157.1, 156.6, 155.5, 152.0, 149.7, 140.8, 140.3, 139.4, 121.3, 118.5, 118.1, 117.7, 109.8, 41.7, 40.8, 33. 2. Elemental analyses found: C%, 49.08; H%, 3.40; N%, 28.92; S%, 7.45. Calc. for $C_{18}H_{14}FN_9O_2S$: C%, 3.21; N%, 28.69; S%, 7.30.

General method for the synthesis of 1,5-disubstituted-(3*Z*)-3-[(2*E*/*Z*)-(1,3-thiazol-2(3*H*)-ylidene) hydrazinylidene]-1,3-dihydro-2*H*-indol-2-one 12a–d and 13a–d

A mixture of appropriate isatin-3-thiosemicarbazones **8a–d**, **9a–d** (1 mmol), chloroacetone (0.09 g, 1 mmol) and anhydrous

sodium acetate (0.16 g, 2 mmol) in ethanol (50 mL) was refluxed for 24 h. The reaction mixture was cooled and poured into crushed ice. The precipitate was filtered and dried to give yellow to orange products. The crude powder was purified by column chromatography on a silica gel column using developing systems (A) as the mobile phase.

1-[2-(4-Oxo-1,5-dihydro-4*H*-pyrazolo[3,4-*d*]pyrimidine-1-yl) ethyl]-(3*Z*)-3-[(2*E*/*Z*)-(1,3-thiazol-2(3*H*)-ylidene)hydrazinylidene]-1,3-dihydro-2*H*-indol-2-one 12a. Yield 0.24 g (59%), reddish brown powder, mp: 223–225 °C, IR: 3435, 3084, 2961, 1694, 1583, 1351, 783. ^{1}H NMR δ: (*E*/*Z*%, 50 : 50): 12.92 (s, 1H, $NH_{(E)}$), 12.44 (s, 1H, $NH_{(Z)}$), 8.70–8.45 (m, $1H_{(E)}$), 8.33–8.15 (m, $1H_{(Z)}$), 8.02–7.96 (m, 3H), 7.75 (m, $1H_{(E)}$), 7.55–7.36 (m, $1H_{(Z)}$), 7.26 (dd, J = 12.8, 7.5 Hz, 1H), 7.17 (dd, J = 13.4, 6.3 Hz, $1H_{(Z)}$), 7.06 (dd, J = 7.1, 3.6 Hz, $1H_{(E)}$), 7.04–6.91 (m, $1H_{(Z)}$), 6.84–6.75 (m, $1H_{(E)}$), 6.68–6.57 (m, $1H_{(Z)}$), 6.49 (s, $1H_{(E)}$), 6.33 (s, $1H_{(Z)}$), 4.53 (d, J = 4.7 Hz, 2H), 4.36–3.97 (m, 2H). ^{13}C NMR δ: $178.5_{(E)}$, $178.1_{(Z)}$, $164.7_{(E)}$, $164.6_{(Z)}$, 156.8, $152.1_{(E)}$, $151.9_{(Z)}$, $150.9_{(E)}$, $150.5_{(Z)}$, 141.9, 136.1, $135.3_{(E)}$, $135.1_{(Z)}$,$130.3_{(E)}$, $130.1_{(Z)}$, 129.8, $126.5_{(E)}$, $126.3_{(Z)}$, $122.2_{(E)}$, $121.9_{(Z)}$, $118.5_{(E)}$, $117.8_{(Z)}$, 108.3, $105.9_{(E)}$, $105.3_{(Z)}$, $102.1_{(E)}$, $101.5_{(Z)}$, 48.3, 44.9. Elemental analyses found: C%, 53.40; H%, 3.59; N%, 27.41; S%, 8.01. Calc. for $C_{18}H_{14}N_8O_2S$: C%, 53.19; H%, 3.47; N%, 27.57; S%, 7.89.

5-Chloro-1-[2-(4-oxo-1,5-dihydro-4*H*-pyrazolo[3,4-*d*] pyrimidine-1-yl)ethyl]-(3*Z*)-3-[(2*E*/*Z*)-(1,3-thiazol-2(3*H*)-ylidene)hydrazinylidene]-1,3-dihydro-2*H*-indol-2-one 12b. Yield 0.29 g (68%), yellowish brown powder, mp 234–237 °C dec., IR: 3444, 3084, 2925, 1694, 1583, 1351, 783. ^{1}H NMR δ *E*/*Z* %, (40 : 60): 12.69 (s, $1H_{(E)}$), 12.06 (s, $1H_{(Z)}$), 8.58–8.38 (m, $1H_{(E)}$), 8.39–7.73 (m, 3H), 7.84–7.50 (m, $1H_{(Z)}$), 7.26 (d, J = 6.3 Hz, 1H), 7.18 (d, J = 6.4 Hz, $1H_{(Z)}$), 7.05 (s, 1H), 6.59 (d, J = 8.8 Hz, 1H), 6.40 (s, 1H) 4.50 (s, 2H), 4.39–3.96 (m, 2H). ^{13}C NMR δ: $178.7_{(E)}$, $178.4_{(Z)}$, $164.1_{(E)}$, $163.9_{(Z)}$, 156.3, 151.6, $150.5_{(E)}$,$150.3_{(Z)}$, 140.1, 135.7, 134.8, $128.4_{(E)}$, $128.2_{(Z)}$, 125.8, $125.5_{(E)}$, $125.4_{(Z)}$, $125.1_{(E)}$, $124.9_{(Z)}$, $118.7_{(E)}$, $118.4_{(Z)}$, 108.8, 105.0, $101.9_{(E)}$, $101.4_{(Z)}$, 45.0, 43.2. Elemental analyses found: C%, 48.79; H%, 3.13; N%, 25.68; S%, 7.41. Calc. for $C_{18}H_{13}ClN_8O_2S$: C%, 49.04; H%, 2.97; N%, 25.42; S%, 7.27.

5-Methoxy-1-[2-(4-oxo-1,5-dihydro-4*H*-pyrazolo[3,4-*d*] pyrimidine-1-yl) ethyl]-(3*Z*)-3-[(2*E*/*Z*)-(1,3-thiazol-2(3*H*)-ylidene) hydrazinylidene]-1,3-dihydro-2*H*-indol-2-one 12c. Yield 0.26 g (61%), reddish brown powder, mp: 226–228 °C dec., IR: 3436, br (NH), 3084 (CH aromatic), 2945, 1694, 1542, 1356, 782. ^{1}H NMR δ: (*E*/*Z*%, 30 : 70): 12.97 (s, $1H_{(E)}$), 12.41 (s, 1H, $NH_{(Z)}$), 8.50–8.30 (m, $1H_{(E)}$), 8.26–7.91 (m, 3H), 7.83–7.55 (m, $1H_{(Z)}$), 7.43 (d, J = 12.6 Hz, 1H $_{(E)}$), 7.02 (d, J = 13.1 Hz, $1H_{(Z)}$), 6.83 (s, $1H_{(E+Z)}$), 6.74 (s, 1H,), 6.56 (s, $1H_{(E)}$), 6.34 (s, $1H_{(Z)}$), 4.52 (s, 2H),4.05–4.18 (m, 2H), 3.75 (s, 3H). ^{13}C NMR δ: $178.4_{(E)}$, $177.6_{(Z)}$, $164.9_{(E)}$, $164.7_{(Z)}$, $157.5_{(E)}$, $156.9_{(Z)}$, 155.7, 155.4, 155.2, 152.4, 152.1, $151.1_{(E)}$, $151.0_{(Z)}$, 136.0, 135.4, 118.8, 114.4, 113.5, 105.6, $101.9_{(E)}$, $101.6_{(Z)}$, 56.1, 45.3, 43.7. Elemental analyses found: C%, 52.43; H%, 3.81; N%, 25.89; S%, 7.52. Calc. for $C_{19}H_{16}N_8O_3S$: C%, 52.29; H%, 3.70; N%, 25.67; S%, 7.35.

5-Fluoro-1-[2-(4-oxo-1,5-dihydro-4*H*-pyrazolo[3,4-*d*] pyrimidine-1-yl) ethyl]-(3*Z*)-3-[(2*E*/*Z*)-(1,3-thiazol-2(3*H*)-ylidene) hydrazinylidene]-1,3-dihydro-2*H*-indol-2-one 12d. Yield 0.22 g (52%), yellowish brown powder, mp 242–246 °C dec., IR: 3435, 3107, 2927, 1697, 1541, 1355, 782. ^{1}H NMR δ (*E*/*Z* %, 35 : 65): 12.59 (s, 1H), 8.37–8.16 (m, $1H_{(E)}$), 8.14–7.89 (m, $4H_{(Z)}$), 7.77 (dd, J = 17.5, 8.4 Hz, 1H), 7.14–6.90 (m, 1H), 6.62 (dd, J = 8.3, 4.0 Hz, 1H), 6.55 (s, $1H_{(E)}$), 6.40 (d, J = 3.1 Hz, $1H_{(Z)}$), 4.51 (d, J = 4.6 Hz, 2H), 4.39–3.89 (m, 2H). ^{13}C NMR δ: 178.7 (C=$O_{(E)}$), 177.6 (C=$O_{(Z)}$), 164.7 (thiazol C=$N_{(E)}$), $164.5_{(Z)}$, $157.2_{(E)}$, $156.9_{(Z)}$, 155.9, 154.8, 152, $151_{(E)}$, $150.8_{(Z)}$, 140.4, 138.7, 138.2, 136.9, 136.2, 135.2, 108.6, 105.4, $102.2_{(E)}$, $101.9_{(Z)}$, 45.4, 45.0. Elemental analyses found: C%, 51.20; H%, 3.23; N%, 26.61; S%, 7.68. Calc. for $C_{18}H_{13}FN_8O_2S$: C%, 50.94; H%, 3.09; N%, 26.40; S%, 7.56.

1-[2-(6-Amionpurine-9-yl)ethyl]-(3*Z*)-3-[(2*E*/*Z*)-(1,3-thiazol-2(3*H*)-ylidene)hydrazinylidene]-1,3-dihydro-2*H*-indol-2-one 13a. Yield 0.23 g (62%), brown powder, mp 249–250 °C dec., IR: 3338, 3181, 3104, 2924, 1682, 1603, 1544, 1329. ^{1}H NMR δ: (*E*/*Z* %, 38 : 62): 12.93 (s, $1H_{(E)}$), 12.44 (s, $1H_{(Z)}$), 8.26 (d, J = 7.4 Hz, $2H_{(E)}$), 8.09 (s, 1H), 8.02 (s, 1H), 7.48 (d, J = 7.3 Hz, $1H_{(Z)}$), 7.24 (t, J = 7.2 Hz, $1H_{(E)}$), 7.15–7.07 (m, 3H), 7.05 (t, J = 7.2 Hz, $1H_{(Z)}$), 6.96 (t, J = 7.5 Hz, $1H_{(E)}$), 6.90 (d, J = 7.9 Hz, 1H), 6.77 (d, J = 8.4 Hz, 1H), 6.51 (s, $1H_{(E)}$), 6.36 (s, $1H_{(Z)}$), 4.44 (dd, J = 13.3, 8.0 Hz, 2H), 4.19 (dd, J = 14.8, 9.5 Hz, 2H). ^{13}C NMR δ: 177.9, 164.3, 155.7, 152.3, 149.8, 141.8, $141.4_{(E)}$, $141.0_{(Z)}$, 137.2, 135.8, $130.0_{(E)}$, $129.5_{(Z)}$, 126.1, $122.9_{(E)}$, $121.9_{(Z)}$, $119.2_{(E)}$, $118.7_{(Z)}$, 117.6, $109.2_{(E)}$ $107.7_{(Z)}$, 101,4, 41.3, 41.1. Elemental analyses found: C%, 53.57; H%, 3.65; N%, 31.30; S%, 7.85. Calc. for $C_{18}H_{15}N_9OS$: C%, 53.32; H%, 3.73; N%, 31.09; S%, 7.91.

1-[2-(6-Amionpurine-9-yl) ethyl]-5-chloro-(3*Z*)-3-[(2*E*/*Z*)-(1,3-thiazol-2(3*H*)-ylidene)hydrazinylidene]-1,3-dihydro-2*H*-indol-2-one 13b. Yield 0.25 g (59%), brownish orange powder, mp 214–215 °C dec., IR: 3365, 3152, 3076, 2926, 1672, 1601, 1545, 1325. ^{1}H NMR δ: 12.70 (s, 1H), 8.28 (s, 1H), 8.05 (s, 1H), 8.01 (s, 1H), 7.79 (s, 1H), 7.15 (d, J = 9.3 Hz, 3H), 6.77 (d, J = 8.3 Hz, 1H), 6.44 (s, 1H), 4.41 (s, 2H), 4.15 (s, 2H). ^{13}C NMR δ: 178.4, 163.9, 155.7, 152.6, 149.7, 140.8, 140.5, 140.2, 135.5, 128.2, 125.6, 125.0, 118.7, 118.6, 108.6, 102.0, 42.6, 41. Elemental analyses, found: C%, 49.42; H%, 3.47; N%, 28.90; S%, 7.41. Calc. for $C_{18}H_{14}ClN_9OS$: C%, 49.15; H%, 3.21; N%, 28.66; S%, 7.29.

1-[2-(6-Amionpurine-9-yl) ethyl]-5-methoxy-(3*Z*)-3-[(2*E*/*Z*)-(1,3-thiazol-2(3*H*)-ylidene)hydrazinylidene]-1,3-dihydro-2*H*-indol-2-one 13c. Yield 0.27 g (64%), dark orange powder, mp: 265–267 °C dec., IR: 3338, 3176, 3108, 2925, 1675, 1598, 1544, 1325. ^{1}H NMR δ: 12.98 (s, $1H_{(E)}$), 12.41 (s, $1H_{(Z)}$), 8.08 (s, 1H), 8.05 (s, $1H_{(E)}$), 8.01 (s, 1H), 7.94 (s, $1H_{(Z)}$), 7.15 (s, 2H), 7.00 (s, 1H), 6.83 (s, 1H), 6.73–6.70 (m, 1H), 6.68 (s, 1H), 4.42 (d, J = 16 Hz, 2H), 4.14 (d, J = 20 Hz, 2H), 3.74 (s, 3H). ^{13}C NMR δ: 177.6, 164.2, 155.7, 154.8, 152.2, 149.6, 140.8, 137.4, 135.5, 135.1, 118.6, 118.2, 113.8, 113.0, 107.9, 101.2, 55.6, 41.1, 40.9. Elemental analyses found: C%, 52.62; H%, 4.18; N%, 29.07; S%, 7.43. Calc. for $C_{19}H_{17}N_9O_2S$: C%, 52.40; H%, 3.93; N%, 28.95; S%, 7.36.

1-[2-(6-Amionpurine-9-yl) ethyl]-5-fluoro-(3*Z*)-3-[(2*E*/*Z*)-(1,3-thiazol-2(3*H*)-ylidene)hydrazinylidene]-1,3-dihydro-2*H*-indol-2-one 13d. Yield 0.26 g (61%), brownish orange powder, mp: 232 °C dec., IR: 3362, 3152, 3067, 2926, 1680, 1599, 1543, 1324. ^{1}H NMR δ: 12.59 (s, 1H), 8.05 (s, 2H), 8.01 (s, 1H), 7.14 (s, 2H), 6.98 (s, 1H), 6.77 (s, 1H), 6.42 (s, 1H,), 4.41 (s, 2H), 4.15 (s, 2H). ^{13}C NMR δ: 178.2, 164.2, 155.7, 152.2, 149.7,140.8, 137.8, 136.3, 135.8, 118.6, 115, 114.8, 112.8, 112.5, 108.3, 101.8, 41.0, 40.8.

Elemental analyses found: C%, 51.27; H%, 3.45; N%, 29.64; S%, 7.49. Calc. for $C_{18}H_{14}FN_9OS$: C%, 51.06; H%, 3.33; N%, 29.77; S%, 7.57.

HPLC purity assessment of compounds 6b, 8b, 12a, 12b, and 12c

The purity of the most active compounds (**6b**, **8b**, **12a**, **12b**, and **12c**) was evaluated using high-performance liquid chromatography (HPLC). Analyses were performed using a reverse-phase C18 column (250 mm × 4.6 mm, 5 μm) at ambient temperature. The mobile phase consisted of phosphate buffer (pH 6), adjusted with 0.1 N NaOH and acetonitrile in a 40 : 60 (v/v) ratio, filtered and degassed before use. The flow rate was set to 1.0 mL min^{-1}, with UV detection at 254 nm. Allopurinol was used as an internal standard in all samples. Purity was quantified by calculating the ratio of the analyte peak area to that of the internal standard. Full chromatographic data are provided in the SI.

Biological investigation

Cell lines. All cell lines were obtained from the American Type Culture Collection (ATCC, Rockville, Maryland, USA) and are maintained at the Hirszfeld Institute of Immunology and Experimental Therapy, Polish Academy of Sciences (Wroclaw, Poland). Enzyme assay studies were conducted at the confirmatory diagnostic unit in VACSERA, Egypt.

Culture media. The HepG2 cell line was cultured in Eagle's medium (IIET PAS, Wroclaw, Poland) containing 10% fetal bovine serum (HyClone, Life Technologies Poland) and 2 mM L-glutamine (Sigma-Aldrich Chemie GmbH, Steinheim, Germany). The MV-4-11 cell line was cultured in RPMI 1640 with a stable glutamine medium (Biowest, Nuaillé, France) containing 10% fetal bovine serum and 1.0 mM sodium pyruvate (both Sigma-Aldrich Chemie GmbH, Steinheim, Germany). All culture media were supplemented with 100 U mL^{-1} penicillin (Polfa Tarchomin S.A., Warsaw, Poland) and 100 μg mL^{-1} streptomycin (Sigma-Aldrich Chemie GmbH, Steinheim, Germany). The cells were grown at 37 °C in a humid atmosphere saturated with 5% CO_2.

Compounds. 7 compounds were tested. Cisplatin (CDDP, Cisplatin 1 mg mL^{-1} Concentrate for Solution for Infusion, Accord Healthcare Poland), the active cytostatic drug, was used as a control. Sunitinib and sorafenib (both from Sigma-Aldrich, Merck, Darmstadt, Germany) were used as positive controls for the compounds. The samples of the compounds were prepared freshly before being added to the cells. Prior to usage, the compounds were weighed and dissolved in DMSO to a concentration of 10 mg mL^{-1} and subsequently diluted in culture medium to reach the required concentration depending on the type of test. Camptothecin (Pol-Aura, Poland) and doxorubicin (Doxorubicin Accord 2 mg mL^{-1}, Accord Healthcare Poland) were used as controls for the caspase-3/7 activity assay. Sunitinib, sorafenib and camptothecin were dissolved in DMSO. All cytostatics were diluted in culture medium to reach the required concentrations depending on the type of test.

Antiproliferative assay

The antiproliferative activity of the tested analogs was evaluated using the SRB assay for adherent cells and the MTT assay for suspension (leukemic) cells. The A-498 cells were seeded at 1500 cells per well, HepG2, BALB/3T3 clone A31 and MV4-11 at 2000 cells per well, MDA-MB-231 at 2500 cells per well in 384-well plates (Greiner Bio-One, Kremsmünster, Austria). After 24 hours, cells were treated with tested compounds (0.1–100 μg mL^{-1}) and incubated for 72 hours at 37 °C with 5% CO_2. For the SRB assay, the cells were fixed with cold 50% (w/v) trichloroacetic acid (Avantor Performance Materials, Gliwice, Poland) and stained with a 0.4% (w/v) solution of sulforhodamine B (Sigma-Aldrich, Germany). Protein-bound dye was extracted from the stained cells with a 10 mM TRIS base (Avantor Performance Materials, Gliwice, Poland) solution, and absorbance was measured at 540 nm using a Biotek Hybrid H4 reader (BioTek Instruments, Inc., Winooski, Vermont, USA). For the MTT assay, MTT solution was added. After 4 h of incubation, formazan crystals were dissolved in DMF solution, and absorbance was recorded at a wavelength of 570 nm. Sorafenib served as a reference, and IC_{50} values were determined using Cheburator 0.4 software. Each compound was tested in triplicate, and the experiments were repeated at least three times.

Cell cycle analysis

Cells (1×10^6) were washed twice with cold PBS and then fixed in 70% ethanol at −20 °C for 24 hours. Following PBS washing, the cells were treated with RNAse (8 mg mL^{-1}, Thermo Scientific, Waltham, MA, USA) at 37 °C for 1 hour. Next, the cells were stained with propidium iodide (0.5 mg mL^{-1}, Sigma-Aldrich Chemie GmbH, Germany) at 4 °C for 30 minutes, and the cellular DNA content was analyzed using BD LSR Fortessa II (Becton Dickinson, San Jose, CA, USA). The percentage of stained cells was calculated using ModFit LT version 3.2 (Verity Software House, USA) and Flowing Software version 2.5.1 (freeware developed by Perttu Terho, Turku Centre for Biotechnology, Finland).

Enzymatic caspase-3/7 activity assay

An enzymatic caspase-3/7 activity assay was conducted using the HepG2 (hepatocellular carcinoma) cell line to evaluate the four test compounds. Cisplatin served as a cytostatic control. Camptothecin and doxorubicin were used as positive controls for the caspase-3/7 activity assay. All test compounds were dissolved in DMSO, diluted in culture medium, and applied to cells seeded in 24-well plates at a density of 1.0×10^5 cells per mL. After a 72 hour treatment, the cells were lysed, and caspase-3/7 activity was measured using Ac-DEVD-ACC as a fluorogenic substrate. Fluorescence was recorded for 2 hours at 37 °C. In parallel, an SRB antiproliferative assay was performed to assess cell viability. After 72 hours of compound exposure, the cells were fixed with trichloroacetic acid and stained with sulforhodamine B, and absorbance was measured at 540 nm. Both assays were conducted in duplicate, and the experiments were repeated three times.

In vitro CDK6 inhibitory assay

CDK6 inhibitory activity was evaluated using the ADP-Glo™ Kinase Assay CDK6 kit (BPS Bioscience, San Diego, CA, USA) following the provided protocol. This assay utilizes the Kinase-Glo® MAX reagent for detection and is formatted in a 96-well plate with sufficient quantities of purified recombinant CDK6/Cyclin D3 enzyme and CDK substrate peptide. The reaction was initiated by adding 20 μL of diluted CDK6/Cyclin D3 enzyme to each well, which contained varying concentrations of test compounds and a test inhibitor control. The plate was then incubated at 30 °C for 45 minutes. After incubation, 50 μL of Kinase-Glo Max reagent was added to each well, and the plate was covered with aluminum foil and incubated at room temperature for an additional 15 minutes. Luminescence was measured using a Tecan Spark reader with an excitation wavelength of 360 nm and an emission wavelength of 450 nm. Blank values were subtracted from all measurements to ensure accuracy.

In vitro VEGFR-2 inhibitory activity assay

VEGFR-2 kinase inhibition was evaluated using the VEGFR-2 Kinase Assay Kit (San Diego, CA, USA) following the manufacturer's protocol (**https://bpsbioscience.com/vegfr2-kdrkinase-assay-kit-40325**). This 96-well format assay utilized Kinase-Glo Max for detection. A master mixture containing kinase buffer, ATP, PTK substrate, and water was prepared and added to each well. Test inhibitor wells received 5 μL of inhibitor solution, while control and blank wells received a solution without the inhibitor. VEGFR-2 enzyme was diluted to 1 ng μL^{-1} and added to test and positive control wells, followed by incubation at 30 °C for 45 minutes. Afterward, Kinase-Glo Max reagent was added, and luminescence was measured using a microplate reader. IC_{50} values were determined using non-linear regression analysis, with results presented as mean IC_{50} (nM) ± SD from at least two independent experiments performed in triplicate.

Xanthine oxidase (XO) inhibition assay

The xanthine oxidase (XO) inhibitory activity of compounds **6b**, **7b**, **8b**, **12a–12c**, and **13b** was evaluated by measuring uric acid production at 292 nm using a spectrophotometric assay. Allopurinol served as a positive control. The reaction mixture comprised 1.5 mL of 50 mM potassium phosphate buffer (pH 7.4), 1 mL of the test compound at varying concentrations, and 0.5 mL of freshly prepared XO enzyme solution. After a 15 minute pre-incubation to allow enzyme–compound complex formation, 1 mL of 0.10 mM xanthine solution was added, followed by 30 minute incubation. The reaction was terminated with 1 mL of 1 M HCl. Control experiments were performed using phosphate buffer instead of the xanthine substrate. All measurements were conducted in triplicate, and the results were reported as IC_{50} values ± standard deviation (SD). Kinetic parameters, including the Michaelis–Menten constant (K_m) and maximum velocity (V_{max}), were determined using either non-linear interpolation of the Michaelis–Menten equation or Lineweaver–Burk plot analysis.

In vitro chemical stability assessment

To investigate chemical stability under simulated physiological conditions, compounds **6b**, **8b**, and **12a–12c** were prepared at 30 μM in phosphate-buffered saline (PBS, pH 7.4) and incubated at 37 ± 0.5 °C. Samples were collected at predetermined intervals (0, 0.5, 1, 2, 4, 6, 8, 10, and 24 h) and analyzed by UV-Vis spectrophotometry across the 190–800 nm range using a 1 cm quartz cuvette. The instrument was blanked with PBS prior to each measurement. Particular attention was given to identifying shifts in the absorption maxima (λ_{max}), variations in absorbance, or new spectral features indicating chemical degradation.

Author contributions

All authors contributed significantly to the work. Gehan Ahmed Abdel Hafez: conducted the synthesis, biological evaluation, data curation, and prepared the original draft of the manuscript. Dagmara Kłopotowska, Beata Filip Psurska, Joanna Wietrzyk: performed biological evaluation and contributed to the experimental work. Ahmed S. Aboraia: carried out data analysis, molecular docking studies, figure preparation, and manuscript editing. Tarek Aboul Fadl: conceptualization, methodology design, supervision, project administration, and critical revision of the manuscript. Adel F. Youssef: conceptualization, supervision, project administration, data analysis, and critical manuscript revision. All authors reviewed and approved the final version of the manuscript.

Conflicts of interest

The authors declare that they have no conflicts of interest regarding the publication of this article.

Data availability

The authors declare that all the data generated or analyzed during this study are included in this manuscript and its SI. See DOI: **https://doi.org/10.1039/d5ra04997k**.

References

1 F. Bray, M. Laversanne, E. Weiderpass and I. Soerjomataram, The ever-increasing importance of cancer as a leading cause of premature death worldwide, *Cancer*, 2021, **127**(16), 3029–3030.
2 S. Chen, Z. Cao, K. Prettner, M. Kuhn, J. Yang, L. Jiao, *et al.*, Estimates and projections of the global economic cost of 29 cancers in 204 countries and territories from 2020 to 2050, *JAMA Oncol.*, 2023, **9**(4), 465–472.
3 Z. Long, Y. Zuo, R. Li, Y. Le, Y. Dong and L. Yan, Design, synthesis and biological evaluation of 4-arylamino-pyrimidine derivatives as focal adhesion kinase inhibitors, *J. Bioorg. Chem.*, 2023, **140**, 106792.
4 L. Ding, J. Cao, W. Lin, H. Chen, X. Xiong, H. Ao, *et al.*, The roles of cyclin-dependent kinases in cell-cycle progression

and therapeutic strategies in human breast cancer, *Int. J. Mol. Sci.*, 2020, **21**(6), 1960.

5 CDK inhibitors from past to present: A new wave of cancer therapy, *Seminars in Cancer Biology*, ed. M. J. Mughal, K. Bhadresha and H. F. Kwok, Elsevier, 2023.

6 M. Yousuf, P. Khan, A. Shamsi, M. Shahbaaz, G. M. Hasan, Q. M. R. Haque, *et al.*, Inhibiting CDK6 activity by quercetin is an attractive strategy for cancer therapy, *ACS Omega*, 2020, **5**(42), 27480–27491.

7 Q.-Y. Chong, Z.-H. Kok, X. Xiang, A. L.-A. Wong, W.-P. Yong, G. Sethi, *et al.*, A unique CDK4/6 inhibitor: current and future therapeutic strategies of abemaciclib, *Pharmacol. Res.*, 2020, **156**, 104686.

8 S. Goel, J. S. Bergholz and J. J. Zhao, Targeting CDK4 and CDK6 in cancer, *Nat. Rev. Cancer*, 2022, **22**(6), 356–372.

9 Q. Hu and T. Huang, Regulation of the cell cycle by ncRNAs affects the efficiency of CDK4/6 inhibition, *Int. J. Mol. Sci.*, 2023, **24**(10), 8939.

10 K. Yuan, X. Wang, H. Dong, W. Min, H. Hao and P. Yang, Selective inhibition of CDK4/6: A safe and effective strategy for developing anticancer drugs, *Acta Pharm. Sin. B*, 2021, **11**(1), 30–54.

11 P. Łukasik, I. Baranowska-Bosiacka, K. Kulczycka and I. Gutowska, Inhibitors of cyclin-dependent kinases: types and their mechanism of action, *Int. J. Mol. Sci.*, 2021, **22**(6), 2806.

12 M. Zhang, L. Zhang, R. Hei, X. Li, H. Cai, X. Wu, *et al.*, CDK inhibitors in cancer therapy, an overview of recent development, *Am. J. Cancer Res.*, 2021, **11**(5), 1913.

13 S. Izadi, M. Hojjat-Farsangi, V. Karpisheh and F. Jadidi-Niaragh, Pan Cyclin-Dependent Kinase Inhibitors for the Treatment of Breast Cancer, *Int. J. Drug Res. Clin.*, 2023, **1**(1), e2–e.

14 J. Sun, S. Liang, X. Liu, S. Zhang, M. Li, Q. Zhang, *et al.*, Insights into the selectivity of a brain-penetrant CDK4/6 vs CDK1/2 inhibitor for glioblastoma used in multiple replica molecular dynamics simulations, *J. Biomol. Struct. Dyn.*, 2023, 1–20.

15 H. A. Abd El-wahab, H. S. Mansour, A. M. Ali, R. El-Awady and T. Aboul-Fadl, New cell cycle checkpoint pathways regulators with 2-Oxo-indoline scaffold as potential anticancer agents: Design, synthesis, biological activities and in silico studies, *Bioorg. Chem.*, 2022, **120**, 105622.

16 J. F. Campos, T. Besson and S. Berteina-Raboin, Review on the Synthesis and Therapeutic Potential of Pyrido [2, 3-d],[3, 2-d],[3, 4-d] and [4, 3-d] pyrimidine Derivatives, *Pharmaceuticals*, 2022, **15**(3), 352.

17 S. Nikhar, I. Siokas, L. Schlicher, S. Lee, M. Gyrd-Hansen, A. Degterev, *et al.*, Design of pyrido [2, 3-d] pyrimidin-7-one inhibitors of receptor interacting protein kinase-2 (RIPK2) and nucleotide-binding oligomerization domain (NOD) cell signaling, *Eur. J. Med. Chem.*, 2021, **215**, 113252.

18 D. Bhurta and S. B. Bharate, Analyzing the scaffold diversity of cyclin-dependent kinase inhibitors and revisiting the clinical and preclinical pipeline, *Med. Res. Rev.*, 2022, **42**(2), 654–709.

19 T. Liang, Y. Yang, J. Wang, Z. Xie and X. Chen, The application of pyrrolo [2, 3-d] pyrimidine scaffold in medicinal chemistry from 2017 to 2021, *Mini-Rev. Med. Chem.*, 2023, **23**(10), 1118–1136.

20 S. Lv, J. Yang, J. Lin, X. Huang, H. Zhao, C. Zhao, *et al.*, CDK4/6 inhibitors in lung cancer: current practice and future directions, *Eur. Respir. Rev.*, 2024, **33**(171), 230145.

21 A. M. Abuzenadah, F. Al-Sayes, S. S. Mahafujul Alam, M. Hoque, S. Karim, I. M. Hussain, *et al.*, Elucidating antiangiogenic potential of Rauwolfia serpentina: VEGFR-2 targeting-based molecular docking study, *J. Evidence-Based Complementary Altern. Med.*, 2022, **2022**(1), 6224666.

22 Y. Liu, Y. Li, Y. Wang, C. Lin, D. Zhang, J. Chen, *et al.*, Recent progress on vascular endothelial growth factor receptor inhibitors with dual targeting capabilities for tumor therapy, *J. Hematol. Oncol.*, 2022, **15**(1), 89.

23 M. Moradi, A. Mousavi, Z. Emamgholipour, J. Giovannini, S. Moghimi, F. Peytam, *et al.*, Quinazoline-based VEGFR-2 inhibitors as potential anti-angiogenic agents: A contemporary perspective of SAR and molecular docking studies, *Eur. J. Med. Chem.*, 2023, 115626.

24 Y. Zuo, R. Li, Y. Zhang, G. Bao, Y. Le, L. Yan, *et al.*, Design, synthesis and antitumor activity of 5-trifluoromethylpyrimidine derivatives as EGFR inhibitors, *J. Enzyme Inhib. Med. Chem.*, 2022, **37**(1), 2742–2754.

25 C.-Y. Huang, Y.-Y. Chang, S.-T. Chang and H.-T. Chang, Xanthine oxidase inhibitory activity and chemical composition of Pistacia chinensis leaf essential oil, *Pharmaceutics*, 2022, **14**(10), 1982.

26 G. Joshi, M. Sharma, S. Kalra, N. S. Gavande, S. Singh and R. J. B. C. Kumar, Design, synthesis, biological evaluation of 3, 5-diaryl-4, 5-dihydro-1H-pyrazole carbaldehydes as non-purine xanthine oxidase inhibitors: Tracing the anticancer mechanism *via* xanthine oxidase inhibition, *Bioorg. Chem.*, 2021, **107**, 104620.

27 Y. Li, T.-T. Cao, S. Guo, Q. Zhong, C.-H. Li, Y. Li, *et al.*, Discovery of novel allopurinol derivatives with anticancer activity and attenuated xanthine oxidase inhibition, *Molecules*, 2016, **21**(6), 771.

28 H. Hassan, S. H. Abbas, E. A. Beshr, H. A. Ezelarab and T. F. Ali, The main biotargets of indole or 2-oxoindole-based hybrids acting as promising antiproliferative agents, *J. Adv. Biomedical Pharm. Sci.*, 2023, **6**(4), 174–183.

29 G. Turhal, B. Demirkan, I. N. Baslilar, N. S. Yuncu, S. N. Baytas and A. Demiroglu-Zergeroglu, Preliminary evaluation of antiproliferative and apoptotic activities of novel indolin-2-one derivatives, *Drug Dev. Res.*, 2024, **85**(5), e22229.

30 M. H. Younis, E. R. Mohammed and H. H. Georgey, 4-Thiazolidinones: A structural motif of great synthetic and biological activities, *ERU. Res. J.*, 2023, **2**(3), 525–540.

31 N. C. Desai, D. J. Jadeja, A. M. Jethawa, I. Ahmad, H. Patel and B. Dave, Design and synthesis of some novel hybrid molecules based on 4-thiazolidinone bearing pyridine-pyrazole scaffolds: molecular docking and molecular dynamics simulations of its major constituent onto DNA gyrase inhibition, *Mol. Diversity*, 2024, **28**(2), 693–709.

32 M. Zokaasadi, E. Altunel, D. L. Dayanidhi, J. B. Mantyh, W. K. Watlington, S. J. McCall, *et al.*, Efficacy of fadraciclib (CYC065), a novel dual CDK2/9 inhibitor, on patient-derived models of colorectal cancer, *J. Clin. Oncol.*, 2024, **42**(16), 3596.

33 W. Zaghary, T. Nasr, A. El-Hameed, T. M. Sakr, D. A. Osman and K. El-Adl, Pyrazolopyrimidines as anticancer agents; syntheses and mode of action, *Al-Azhar J. Pharm. Sci.*, 2024, **69**(1), 62–107.

34 D. Adel, K. El-Adl, T. Nasr, T. M. Sakr and W. Zaghary, Pyrazolo [3, 4-d] pyrimidine derivatives as EGFRT790M and VEGFR-2 dual TK inhibitors: Design, synthesis, molecular docking, ADMET profile and anticancer evaluations, *J. Mol. Struct.*, 2023, **1291**, 136047.

35 P. Chen, N. V. Lee, W. Hu, M. Xu, R. A. Ferre, H. Lam, *et al.*, Spectrum and degree of CDK drug interactions predicts clinical performance, *Mol. Cancer Ther.*, 2016, **15**(10), 2273–2281.

36 D. Adel, K. El-Adl, T. Nasr, T. M. Sakr and W. Zaghary, Pyrazolo [3, 4-d] pyrimidine derivatives as EGFRT790M and VEGFR-2 dual TK inhibitors: Design, synthesis, molecular docking, ADMET profile and anticancer evaluations, *J. Mol. Struct.*, 2023, **1291**, 136047.

37 M. Moradi, A. Mousavi, Z. Emamgholipour, J. Giovannini, S. Moghimi, F. Peytam, *et al.*, Quinazoline-based VEGFR-2 inhibitors as potential anti-angiogenic agents: A contemporary perspective of SAR and molecular docking studies, *Eur. J. Med. Chem.*, 2023, 115626.

38 K. Okamoto, M. Ikemori-Kawada, A. Jestel, K. von König, Y. Funahashi, T. Matsushima, *et al.*, Distinct binding mode of multikinase inhibitor lenvatinib revealed by biochemical characterization, *ACS Med. Chem. Lett.*, 2015, **6**(1), 89–94.

39 A. Hassan, M. Badr, D. Abdelhamid, H. A. Hassan, M. A. Abourehab and G. E. D. A. Abuo-Rahma, Design, synthesis, *in vitro* antiproliferative evaluation and *in silico* studies of new VEGFR-2 inhibitors based on 4-piperazinylquinolin-2 (1H)-one scaffold, *Bioorg. Chem.*, 2022, **120**, 105631.

40 E. Kohli, R. Arora and R. Kakkar, Theoretical study of the stability of tautomers and conformers of isatin-3-thiosemicarbazone (IBT), *Can. Chem. Trans.*, 2014, **2**(3), 327–342.

41 N. Shahi, P. N. Yadav, U. Chaudhary, M. Saad, K. Mahiya, A. Khan, *et al.*, 5-Methoxyisatin N (4)-Pyrrolidinyl Thiosemicarbazone (MeOIstPyrd) Restores Mutant p53 and Inhibits the Growth of Skin Cancer Cells, In Vitro, *ACS Omega*, 2023, **8**(35), 31998–32016.

42 G. Caron, J. Kihlberg and G. Ermondi, Intramolecular hydrogen bonding: An opportunity for improved design in medicinal chemistry, *Med. Res. Rev.*, 2019, **39**(5), 1707–1729.

43 S. Tadesse, M. Yu, L. B. Mekonnen, F. Lam, S. Islam, K. Tomusange, *et al.*, Highly potent, selective, and orally bioavailable 4-thiazol-*N*-(pyridin-2-yl) pyrimidin-2-amine cyclin-dependent kinases 4 and 6 inhibitors as anticancer drug candidates: design, synthesis, and evaluation, *J. Med. Chem.*, 2017, **60**(5), 1892–1915.

44 M. Asadi, S. Taghizadeh, E. Kaviani, O. Vakili, M. Taheri-Anganeh, M. Tahamtan, *et al.*, Caspase-3: structure, function, and biotechnological aspects, *Biotechnol. Appl. Biochem.*, 2022, **69**(4), 1633–1645.

45 S. Jin, H.-J. Park, Y. N. Oh, H. J. Kwon, J.-H. Kim, Y. H. Choi, *et al.*, Anti-cancer activity of Osmanthus matsumuranus extract by inducing G2/M arrest and apoptosis in human hepatocellular carcinoma Hep G2 cells, *J. Cancer Prev.*, 2015, **20**(4), 241.

46 U. Takahama, Y. Koga, S. Hirota and R. Yamauchi, Inhibition of xanthine oxidase activity by an oxathiolanone derivative of quercetin, *Food Chem.*, 2011, **126**(4), 1808–1811.

47 M. E. M. B. de Araújo, Y. E. M. Franco, T. G. Alberto, M. C. F. Messias, C. W. Leme, A. C. H. F. Sawaya, *et al.*, Kinetic study on the inhibition of xanthine oxidase by acylated derivatives of flavonoids synthesised enzymatically, *J. Enzyme Inhib. Med. Chem.*, 2017, **32**(1), 978–985.

48 D. Kumar, G. Kaur, A. Negi, S. Kumar, S. Singh and R. Kumar, Synthesis and xanthine oxidase inhibitory activity of 5, 6-dihydropyrazolo/pyrazolo [1, 5-c] quinazoline derivatives, *Bioorg. Chem.*, 2014, **57**, 57–64.

49 R. Rullo, C. Cerchia, R. Nasso, V. Romanelli, E. D. Vendittis, M. Masullo, *et al.*, Novel reversible inhibitors of xanthine oxidase targeting the active site of the enzyme, *Antioxidants*, 2023, **12**(4), 825.

50 P. T. V. Nguyen, T. Van Dat, S. Mizukami, D. L. H. Nguyen, F. Mosaddeque, S. N. Kim, *et al.*, 2D-quantitative structure–activity relationships model using PLS method for anti-malarial activities of anti-haemozoin compounds, *Malar. J.*, 2021, **20**, 1–15.

51 N. Yellasubbaiah and V. Velmurugan, QSAR Modeling, Molecular Docking, and ADME Studies of Novel 5-Oxo-Imidazoline Derivatives as Anti-Breast Cancer Drug Compounds against MCF-7 Cell Line, *J. Med. Chem. Sci.*, 2023, **6**, 3087–3112.

52 M. Lahyaoui, H. El-Idrissi, T. Saffaj, B. Ihssane, N. Saffaj, R. Mamouni, *et al.*, QSAR modeling, molecular docking and molecular dynamic simulation of phosphorus-substituted quinoline derivatives as topoisomerase I inhibitors, *Arabian J. Chem.*, 2023, **16**(6), 104783.

53 M. A. Ismail, A. Negm, R. K. Arafa, E. Abdel-Latif and W. M. El-Sayed, Anticancer activity, dual prooxidant/antioxidant effect and apoptosis induction profile of new bichalcophene-5-carboxamidines, *Eur. J. Med. Chem.*, 2019, **169**, 76–88.

54 M. Suhasini, E. Sailatha, S. Gunasekaran and G. Ramkumaar, Vibrational and electronic investigations, thermodynamic parameters, HOMO and LUMO analysis on Lornoxicam by density functional theory, *J. Mol. Struct.*, 2015, **1100**, 116–128.

55 A. S. Rajpurohit, R. Rajesh, R. R. Muhamed, M. Jaccob, A. J. A. Baskar and V. J. H. Kannappan, DFT investigation of role of N–H···O and N–H···π interactions in the stabilization of the hydrogen bonded complexes of anisole with aromatic amines, *Heliyon*, 2019, **5**(7), e02155.

56 J. M. Aceves-Hernández, M. Inés Nicolás Vázquez, J. Luis Garza Rivera, A. Espinoza Godínez, J. Mateo Flores, J. de Jesús Cruz Guzmán, *et al.*, Palbociclib (PD 0332991) Interaction with Kinases. Theoretical and Comparative Molecular Docking Study, *Chem. Biodiversity*, 2023, **20**(3), e202200554.

57 S. Gul, F. Jan, A. Alam, A. Shakoor, A. Khan, A. F. AlAsmari, *et al.*, Synthesis, molecular docking and DFT analysis of novel bis-Schiff base derivatives with thiobarbituric acid for α-glucosidase inhibition assessment, *Sci. Rep.*, 2024, **14**(1), 3419.

58 **https://www.molinpiration.com/cgi-bin/properties**, June, 2024.

59 D. F. Veber, S. R. Johnson, H.-Y. Cheng, B. R. Smith, K. W. Ward and K. D. Kopple, Molecular properties that influence the oral bioavailability of drug candidates, *J. Med. Chem.*, 2002, **45**(12), 2615–2623.

60 J. C. Phillips, D. J. Hardy, J. D. Maia, J. E. Stone, J. V. Ribeiro, R. C. Bernardi, *et al.*, Scalable molecular dynamics on CPU and GPU architectures with NAMD, *J. Chem. Phys.*, 2020, **153**(4), 044130.

61 B. K. Chagaleti, V. Saravanan, C. Vellapandian and M. K. Kathiravan, Exploring cyclin-dependent kinase inhibitors: a comprehensive study in search of CDK-6 inhibitors using a pharmacophore modelling and dynamics approach, *RSC Adv.*, 2023, **13**(48), 33770–33785.

62 A. Bogdanov, A. Sirazieva, A. Voloshina, T. Abzalilov, A. Samorodov and V. Mironov, Synthesis and antimicrobial, antiplatelet, and anticoagulant activities of new isatin derivatives containing a hetero-fused imidazole fragment, *Russ. J. Org. Chem.*, 2022, **58**(3), 327–334.